Measurement of $e^+e^- \to \pi^+\pi^- D^+ D^-$ cross sections at center-of-mass energies from 4.190 to 4.946 GeV

M. Ablikim,[1] M. N. Achasov,[11,b] P. Adlarson,[69] M. Albrecht,[4] R. Aliberti,[30] A. Amoroso,[68a,68c] M. R. An,[34] Q. An,[65,52] X. H. Bai,[60] Y. Bai,[51] O. Bakina,[31] R. Baldini Ferroli,[25a] I. Balossino,[26a] Y. Ban,[41,g] V. Batozskaya,[1,39] D. Becker,[30] K. Begzsuren,[28] N. Berger,[30] M. Bertani,[25a] D. Bettoni,[26a] F. Bianchi,[68a,68c] J. Bloms,[62] A. Bortone,[68a,68c] I. Boyko,[31] R. A. Briere,[5] A. Brueggemann,[62] H. Cai,[70] X. Cai,[1,52] A. Calcaterra,[25a] G. F. Cao,[1,57] N. Cao,[1,57] S. A. Cetin,[56a] J. F. Chang,[1,52] W. L. Chang,[1,57] G. Chelkov,[31,a] C. Chen,[38] Chao Chen,[49] G. Chen,[1] H. S. Chen,[1,57] M. L. Chen,[1,52] S. J. Chen,[37] S. M. Chen,[55] T. Chen,[1] X. R. Chen,[27,57] X. T. Chen,[1] Y. B. Chen,[1,52] Z. J. Chen,[22,h] W. S. Cheng,[68c] S. K. Choi,[49] X. Chu,[38] G. Cibinetto,[26a] F. Cossio,[68c] J. J. Cui,[44] H. L. Dai,[1,52] J. P. Dai,[72] A. Dbeyssi,[16] R. E. de Boer,[4] D. Dedovich,[31] Z. Y. Deng,[1] A. Denig,[30] I. Denysenko,[31] M. Destefanis,[68a,68c] F. De Mori,[68a,68c] Y. Ding,[35] J. Dong,[1,52] L. Y. Dong,[1,57] M. Y. Dong,[1,52,57] X. Dong,[70] S. X. Du,[74] P. Egorov,[31,a] Y. L. Fan,[70] J. Fang,[1,52] S. S. Fang,[1,57] W. X. Fang,[1] Y. Fang,[1] R. Farinelli,[26a] L. Fava,[68b,68c] F. Feldbauer,[4] G. Felici,[25a] C. Q. Feng,[65,52] J. H. Feng,[53] K. Fischer,[63] M. Fritsch,[4] C. Fritzsch,[62] C. D. Fu,[1] H. Gao,[57] Y. N. Gao,[41,g] Yang Gao,[65,52] S. Garbolino,[68c] I. Garzia,[26a,26b] P. T. Ge,[70] Z. W. Ge,[37] C. Geng,[53] E. M. Gersabeck,[61] A. Gilman,[63] L. Gong,[35] W. X. Gong,[1,52] W. Gradl,[30] M. Greco,[68a,68c] L. M. Gu,[37] M. H. Gu,[1,52] Y. T. Gu,[13] C. Y. Guan,[1,57] A. Q. Guo,[27,57] L. B. Guo,[36] R. P. Guo,[43] Y. P. Guo,[10,f] A. Guskov,[31,a] T. T. Han,[44] W. Y. Han,[34] X. Q. Hao,[17] F. A. Harris,[59] K. K. He,[49] K. L. He,[1,57] F. H. Heinsius,[4] C. H. Heinz,[30] Y. K. Heng,[1,52,57] C. Herold,[54] M. Himmelreich,[30,d] G. Y. Hou,[1,57] Y. R. Hou,[57] Z. L. Hou,[1] H. M. Hu,[1,57] J. F. Hu,[50,i] T. Hu,[1,52,57] Y. Hu,[1] G. S. Huang,[65,52] K. X. Huang,[53] L. Q. Huang,[27,57] L. Q. Huang,[66] X. T. Huang,[44] Y. P. Huang,[1] Z. Huang,[41,g] T. Hussain,[67] N. Hüsken,[24,30] W. Imoehl,[24] M. Irshad,[65,52] J. Jackson,[24] S. Jaeger,[4] S. Janchiv,[28] E. Jang,[49] J. H. Jeong,[49] Q. Ji,[1] Q. P. Ji,[17] X. B. Ji,[1,57] X. L. Ji,[1,52] Y. Y. Ji,[44] Z. K. Jia,[65,52] H. B. Jiang,[44] S. S. Jiang,[34] X. S. Jiang,[1,52,57] Y. Jiang,[57] J. B. Jiao,[44] Z. Jiao,[20] S. Jin,[37] Y. Jin,[60] M. Q. Jing,[1,57] T. Johansson,[69] N. Kalantar-Nayestanaki,[58] X. S. Kang,[35] R. Kappert,[58] M. Kavatsyuk,[58] B. C. Ke,[74] I. K. Keshk,[4] A. Khoukaz,[62] P. Kiese,[30] R. Kiuchi,[1] L. Koch,[32] O. B. Kolcu,[56a] B. Kopf,[4] M. Kuemmel,[4] M. Kuessner,[4] A. Kupsc,[39,69] W. Kühn,[32] J. J. Lane,[61] J. S. Lange,[32] P. Larin,[16] A. Lavania,[23] L. Lavezzi,[68a,68c] Z. H. Lei,[65,52] H. Leithoff,[30] M. Lellmann,[30] T. Lenz,[30] C. Li,[42] C. Li,[38] C. H. Li,[34] Cheng Li,[65,52] D. M. Li,[74] F. Li,[1,52] G. Li,[1] H. Li,[46] H. Li,[65,52] H. B. Li,[1,57] H. J. Li,[17] H. N. Li,[50,i] J. Q. Li,[4] J. S. Li,[53] J. W. Li,[44] Ke Li,[1] L. J. Li,[1] L. K. Li,[1] Lei Li,[3] M. H. Li,[38] P. R. Li,[33,j,k] S. X. Li,[10] S. Y. Li,[55] T. Li,[44] W. D. Li,[1,57] W. G. Li,[1] X. H. Li,[65,52] X. L. Li,[44] Xiaoyu Li,[1,57] H. Liang,[1,57] H. Liang,[65,52] H. Liang,[29] Y. F. Liang,[48] Y. T. Liang,[27,57] G. R. Liao,[12] L. Z. Liao,[44] J. Libby,[23] A. Limphirat,[54] C. X. Lin,[53] D. X. Lin,[27,57] T. Lin,[1] B. J. Liu,[1] C. X. Liu,[1] D. Liu,[16,65] F. H. Liu,[47] Fang Liu,[1] Feng Liu,[6] G. M. Liu,[50,i] H. Liu,[33,j,k] H. B. Liu,[13] H. M. Liu,[1,57] Huanhuan Liu,[1] Huihui Liu,[18] J. B. Liu,[65,52] J. L. Liu,[66] J. Y. Liu,[1,57] K. Liu,[1] K. Y. Liu,[35] Ke Liu,[19] L. Liu,[65,52] Lu Liu,[38] M. H. Liu,[10,f] P. L. Liu,[1] Q. Liu,[57] S. B. Liu,[65,52] T. Liu,[10,f] W. K. Liu,[38] W. M. Liu,[65,52] X. Liu,[33,j,k] Y. Liu,[33,j,k] Y. B. Liu,[38] Z. A. Liu,[1,52,57] Z. Q. Liu,[44] X. C. Lou,[1,52,57] F. X. Lu,[53] H. J. Lu,[20] J. G. Lu,[1,52] X. L. Lu,[1] Y. Lu,[7] Y. P. Lu,[1,52] Z. H. Lu,[1] C. L. Luo,[36] M. X. Luo,[73] T. Luo,[10,f] X. L. Luo,[1,52] X. R. Lyu,[57] Y. F. Lyu,[38] F. C. Ma,[35] H. L. Ma,[1] L. L. Ma,[44] M. M. Ma,[1,57] Q. M. Ma,[1] R. Q. Ma,[1,57] R. T. Ma,[57] X. Y. Ma,[1,52] Y. Ma,[41,g] F. E. Maas,[16] M. Maggiora,[68a,68c] S. Maldaner,[4] S. Malde,[63] Q. A. Malik,[67] A. Mangoni,[25b] Y. J. Mao,[41,g] Z. P. Mao,[1] S. Marcello,[68a,68c] Z. X. Meng,[60] G. Mezzadri,[26a] H. Miao,[1] T. J. Min,[37] R. E. Mitchell,[24] X. H. Mo,[1,52,57] N. Yu. Muchnoi,[11,b] Y. Nefedov,[31] F. Nerling,[16,d] I. B. Nikolaev,[11,b] Z. Ning,[1,52] S. Nisar,[9,l] Y. Niu,[44] S. L. Olsen,[57] Q. Ouyang,[1,52,57] S. Pacetti,[25b,25c] X. Pan,[10,f] Y. Pan,[51] A. Pathak,[1] A. Pathak,[29] M. Pelizaeus,[4] H. P. Peng,[65,52] J. Pettersson,[69] J. L. Ping,[36] R. G. Ping,[1,57] S. Plura,[30] S. Pogodin,[31] V. Prasad,[65,52] F. Z. Qi,[1] H. Qi,[65,52] H. R. Qi,[55] M. Qi,[37] T. Y. Qi,[10,f] S. Qian,[1,52] W. B. Qian,[57] Z. Qian,[53] C. F. Qiao,[57] J. J. Qin,[66] L. Q. Qin,[12] X. P. Qin,[10,f] X. S. Qin,[44] Z. H. Qin,[1,52] J. F. Qiu,[1] S. Q. Qu,[38] K. H. Rashid,[67] C. F. Redmer,[30] K. J. Ren,[34] A. Rivetti,[68c] V. Rodin,[58] M. Rolo,[68c] G. Rong,[1,57] Ch. Rosner,[16] S. N. Ruan,[38] H. S. Sang,[65] A. Sarantsev,[31,c] Y. Schelhaas,[30] C. Schnier,[4] K. Schoenning,[69] M. Scodeggio,[26a,26b] K. Y. Shan,[10,f] W. Shan,[21] X. Y. Shan,[65,52] J. F. Shangguan,[49] L. G. Shao,[1,57] M. Shao,[65,52] C. P. Shen,[10,f] H. F. Shen,[1,57] X. Y. Shen,[1,57] B. A. Shi,[57] H. C. Shi,[65,52] J. Y. Shi,[1] q. q. Shi,[49] R. S. Shi,[1,57] X. Shi,[1,52] X. D. Shi,[65,52] J. J. Song,[17] W. M. Song,[29,1] Y. X. Song,[41,g] S. Sosio,[68a,68c] S. Spataro,[68a,68c] F. Stieler,[30] K. X. Su,[70] P. P. Su,[49] Y. J. Su,[57] G. X. Sun,[1] H. Sun,[57] H. K. Sun,[1] J. F. Sun,[17] L. Sun,[70] S. S. Sun,[1,57] T. Sun,[1,57] W. Y. Sun,[29] X. Sun,[22,h] Y. J. Sun,[65,52] Y. Z. Sun,[1] Z. T. Sun,[44] Y. H. Tan,[70] Y. X. Tan,[65,52] C. J. Tang,[48] G. Y. Tang,[1] J. Tang,[53] L. Y. Tao,[66] Q. T. Tao,[22,h] M. Tat,[63] J. X. Teng,[65,52] V. Thoren,[69] W. H. Tian,[46] Y. Tian,[27,57] I. Uman,[56b] B. Wang,[1] B. L. Wang,[57] C. W. Wang,[37] D. Y. Wang,[41,g] F. Wang,[66] H. J. Wang,[33,j,k] H. P. Wang,[1,57] K. Wang,[1,52] L. L. Wang,[1] M. Wang,[44] M. Z. Wang,[41,g] Meng Wang,[1,57] S. Wang,[10,f] S. Wang,[12] T. Wang,[10,f] T. J. Wang,[38] W. Wang,[53] W. H. Wang,[70] W. P. Wang,[65,52] X. Wang,[41,g] X. F. Wang,[33,j,k] X. L. Wang,[10,f] Y. D. Wang,[40] Y. F. Wang,[1,52,57] Y. H. Wang,[42] Y. Q. Wang,[1] Yaqian Wang,[15,1] Yi Wang,[55] Z. Wang,[1,52] Z. Y. Wang,[1,57] Ziyi Wang,[57] D. H. Wei,[12] F. Weidner,[62] S. P. Wen,[1] D. J. White,[61] U. Wiedner,[4] G. Wilkinson,[63] M. Wolke,[69] L. Wollenberg,[4] J. F. Wu,[1,57] L. H. Wu,[1] L. J. Wu,[1,57] X. Wu,[10,f] X. H. Wu,[29] Y. Wu,[65] Z. Wu,[1,52] L. Xia,[65,52] T. Xiang,[41,g] D. Xiao,[33,j,k] G. Y. Xiao,[37]

H. Xiao,[10,f] S. Y. Xiao,[1] Y. L. Xiao,[10,f] Z. J. Xiao,[36] C. Xie,[37] X. H. Xie,[41,g] Y. Xie,[44] Y. G. Xie,[1,52] Y. H. Xie,[6] Z. P. Xie,[65,52] T. Y. Xing,[1,57] C. F. Xu,[1] C. J. Xu,[53] G. F. Xu,[1] H. Y. Xu,[60] Q. J. Xu,[14] S. Y. Xu,[64] X. P. Xu,[49] Y. C. Xu,[57] Z. P. Xu,[37] F. Yan,[10,f] L. Yan,[10,f] W. B. Yan,[65,52] W. C. Yan,[74] H. J. Yang,[45,e] H. L. Yang,[29] H. X. Yang,[1] L. Yang,[46] S. L. Yang,[57] Tao Yang,[1] Y. F. Yang,[38] Y. X. Yang,[1,57] Yifan Yang,[1,57] M. Ye,[1,52] M. H. Ye,[8] J. H. Yin,[1] Z. Y. You,[53] B. X. Yu,[1,52,57] C. X. Yu,[38] G. Yu,[1,57] T. Yu,[66] X. D. Yu,[41,g] C. Z. Yuan,[1,57] L. Yuan,[2] S. C. Yuan,[1] X. Q. Yuan,[1] Y. Yuan,[1,57] Z. Y. Yuan,[53] C. X. Yue,[34] A. A. Zafar,[67] F. R. Zeng,[44] X. Zeng,[6] Y. Zeng,[22,h] Y. H. Zhan,[53] A. Q. Zhang,[1] B. L. Zhang,[1] B. X. Zhang,[1] D. H. Zhang,[38] G. Y. Zhang,[17] H. Zhang,[65] H. H. Zhang,[53] H. H. Zhang,[29] H. Y. Zhang,[1,52] J. L. Zhang,[71] J. Q. Zhang,[36] J. W. Zhang,[1,52,57] J. X. Zhang,[33,j,k] J. Y. Zhang,[1] J. Z. Zhang,[1,57] Jianyu Zhang,[1,57] Jiawei Zhang,[1,57] L. M. Zhang,[55] L. Q. Zhang,[53] Lei Zhang,[37] P. Zhang,[1] Q. Y. Zhang,[34,74] Shulei Zhang,[22,h] X. D. Zhang,[40] X. M. Zhang,[1] X. Y. Zhang,[44] X. Y. Zhang,[49] Y. Zhang,[63] Y. T. Zhang,[74] Y. H. Zhang,[1,52] Yan Zhang,[65,52] Yao Zhang,[1] Z. H. Zhang,[1] Z. Y. Zhang,[38] Z. Y. Zhang,[70] G. Zhao,[1] J. Zhao,[34] J. Y. Zhao,[1,57] J. Z. Zhao,[1,52] Lei Zhao,[65,52] Ling Zhao,[1] M. G. Zhao,[38] Q. Zhao,[1] S. J. Zhao,[74] Y. B. Zhao,[1,52] Y. X. Zhao,[27,57] Z. G. Zhao,[65,52] A. Zhemchugov,[31,a] B. Zheng,[66] J. P. Zheng,[1,52] Y. H. Zheng,[57] B. Zhong,[36] C. Zhong,[66] X. Zhong,[53] H. Zhou,[44] L. P. Zhou,[1,57] X. Zhou,[70] X. K. Zhou,[57] X. R. Zhou,[65,52] X. Y. Zhou,[34] Y. Z. Zhou,[10,f] J. Zhu,[38] K. Zhu,[1] K. J. Zhu,[1,52,57] L. X. Zhu,[57] S. H. Zhu,[64] S. Q. Zhu,[37] T. J. Zhu,[71] W. J. Zhu,[10,f] Y. C. Zhu,[65,52] Z. A. Zhu,[1,57] B. S. Zou,[1] and J. H. Zou[1]

(BESIII Collaboration)

[1]*Institute of High Energy Physics, Beijing 100049, People's Republic of China*
[2]*Beihang University, Beijing 100191, People's Republic of China*
[3]*Beijing Institute of Petrochemical Technology, Beijing 102617, People's Republic of China*
[4]*Bochum Ruhr-University, D-44780 Bochum, Germany*
[5]*Carnegie Mellon University, Pittsburgh, Pennsylvania 15213, USA*
[6]*Central China Normal University, Wuhan 430079, People's Republic of China*
[7]*Central South University, Changsha 410083, People's Republic of China*
[8]*China Center of Advanced Science and Technology, Beijing 100190, People's Republic of China*
[9]*COMSATS University Islamabad, Lahore Campus, Defence Road, Off Raiwind Road, Lahore 54000, Pakistan*
[10]*Fudan University, Shanghai 200433, People's Republic of China*
[11]*G.I. Budker Institute of Nuclear Physics SB RAS (BINP), Novosibirsk 630090, Russia*
[12]*Guangxi Normal University, Guilin 541004, People's Republic of China*
[13]*Guangxi University, Nanning 530004, People's Republic of China*
[14]*Hangzhou Normal University, Hangzhou 310036, People's Republic of China*
[15]*Hebei University, Baoding 071002, People's Republic of China*
[16]*Helmholtz Institute Mainz, Staudinger Weg 18, D-55099 Mainz, Germany*
[17]*Henan Normal University, Xinxiang 453007, People's Republic of China*
[18]*Henan University of Science and Technology, Luoyang 471003, People's Republic of China*
[19]*Henan University of Technology, Zhengzhou 450001, People's Republic of China*
[20]*Huangshan College, Huangshan 245000, People's Republic of China*
[21]*Hunan Normal University, Changsha 410081, People's Republic of China*
[22]*Hunan University, Changsha 410082, People's Republic of China*
[23]*Indian Institute of Technology Madras, Chennai 600036, India*
[24]*Indiana University, Bloomington, Indiana 47405, USA*
[25a]*INFN Laboratori Nazionali di Frascati, I-00044 Frascati, Italy*
[25b]*INFN Sezione di Perugia, I-06100 Perugia, Italy*
[25c]*University of Perugia, I-06100 Perugia, Italy*
[26a]*INFN Sezione di Ferrara, I-44122 Ferrara, Italy*
[26b]*University of Ferrara, I-44122 Ferrara, Italy*
[27]*Institute of Modern Physics, Lanzhou 730000, People's Republic of China*
[28]*Institute of Physics and Technology, Peace Avenue 54B, Ulaanbaatar 13330, Mongolia*
[29]*Jilin University, Changchun 130012, People's Republic of China*
[30]*Johannes Gutenberg University of Mainz, Johann-Joachim-Becher-Weg 45, D-55099 Mainz, Germany*
[31]*Joint Institute for Nuclear Research, 141980 Dubna, Moscow region, Russia*
[32]*Justus-Liebig-Universitaet Giessen, II. Physikalisches Institut, Heinrich-Buff-Ring 16, D-35392 Giessen, Germany*
[33]*Lanzhou University, Lanzhou 730000, People's Republic of China*
[34]*Liaoning Normal University, Dalian 116029, People's Republic of China*
[35]*Liaoning University, Shenyang 110036, People's Republic of China*
[36]*Nanjing Normal University, Nanjing 210023, People's Republic of China*

[37]Nanjing University, Nanjing 210093, People's Republic of China
[38]Nankai University, Tianjin 300071, People's Republic of China
[39]National Centre for Nuclear Research, Warsaw 02-093, Poland
[40]North China Electric Power University, Beijing 102206, People's Republic of China
[41]Peking University, Beijing 100871, People's Republic of China
[42]Qufu Normal University, Qufu 273165, People's Republic of China
[43]Shandong Normal University, Jinan 250014, People's Republic of China
[44]Shandong University, Jinan 250100, People's Republic of China
[45]Shanghai Jiao Tong University, Shanghai 200240, People's Republic of China
[46]Shanxi Normal University, Linfen 041004, People's Republic of China
[47]Shanxi University, Taiyuan 030006, People's Republic of China
[48]Sichuan University, Chengdu 610064, People's Republic of China
[49]Soochow University, Suzhou 215006, People's Republic of China
[50]South China Normal University, Guangzhou 510006, People's Republic of China
[51]Southeast University, Nanjing 211100, People's Republic of China
[52]State Key Laboratory of Particle Detection and Electronics,
Beijing 100049, Hefei 230026, People's Republic of China
[53]Sun Yat-Sen University, Guangzhou 510275, People's Republic of China
[54]Suranaree University of Technology, University Avenue 111, Nakhon Ratchasima 30000, Thailand
[55]Tsinghua University, Beijing 100084, People's Republic of China
[56a]Turkish Accelerator Center Particle Factory Group, Istinye University, 34010 Istanbul, Turkey
[56b]Turkish Accelerator Center Particle Factory Group, Near East University,
Nicosia, North Cyprus, 99138, Mersin 10, Turkey
[57]University of Chinese Academy of Sciences, Beijing 100049, People's Republic of China
[58]University of Groningen, NL-9747 AA Groningen, Netherlands
[59]University of Hawaii, Honolulu, Hawaii 96822, USA
[60]University of Jinan, Jinan 250022, People's Republic of China
[61]University of Manchester, Oxford Road, Manchester M13 9PL, United Kingdom
[62]University of Muenster, Wilhelm-Klemm-Strasse 9, 48149 Muenster, Germany
[63]University of Oxford, Keble Rd, Oxford OX13RH, United Kingdom
[64]University of Science and Technology Liaoning, Anshan 114051, People's Republic of China
[65]University of Science and Technology of China, Hefei 230026, People's Republic of China
[66]University of South China, Hengyang 421001, People's Republic of China
[67]University of the Punjab, Lahore-54590, Pakistan
[68a]University of Turin, I-10125 Turin, Italy
[68b]University of Eastern Piedmont, I-15121 Alessandria, Italy
[68c]INFN, I-10125 Turin, Italy
[69]Uppsala University, Box 516, SE-75120 Uppsala, Sweden
[70]Wuhan University, Wuhan 430072, People's Republic of China
[71]Xinyang Normal University, Xinyang 464000, People's Republic of China
[72]Yunnan University, Kunming 650500, People's Republic of China
[73]Zhejiang University, Hangzhou 310027, People's Republic of China
[74]Zhengzhou University, Zhengzhou 450001, People's Republic of China

(Received 29 July 2022; accepted 12 September 2022; published 29 September 2022)

[a]Also at the Moscow Institute of Physics and Technology, Moscow 141700, Russia.
[b]Also at the Novosibirsk State University, Novosibirsk 630090, Russia.
[c]Also at the NRC "Kurchatov Institute," PNPI, 188300 Gatchina, Russia.
[d]Also at Goethe University Frankfurt, 60323 Frankfurt am Main, Germany.
[e]Also at Key Laboratory for Particle Physics, Astrophysics and Cosmology, Ministry of Education; Shanghai Key Laboratory for Particle Physics and Cosmology; Institute of Nuclear and Particle Physics, Shanghai 200240, People's Republic of China.
[f]Also at Key Laboratory of Nuclear Physics and Ion-beam Application (MOE) and Institute of Modern Physics, Fudan University, Shanghai 200443, People's Republic of China.
[g]Also at State Key Laboratory of Nuclear Physics and Technology, Peking University, Beijing 100871, People's Republic of China.
[h]Also at School of Physics and Electronics, Hunan University, Changsha 410082, China.
[i]Also at Guangdong Provincial Key Laboratory of Nuclear Science, Institute of Quantum Matter, South China Normal University, Guangzhou 510006, China.
[j]Also at Frontiers Science Center for Rare Isotopes, Lanzhou University, Lanzhou 730000, People's Republic of China.
[k]Also at Lanzhou Center for Theoretical Physics, Lanzhou University, Lanzhou 730000, People's Republic of China.
[l]Also at the Department of Mathematical Sciences, IBA, Karachi, Pakistan.

Using data samples collected with the BESIII detector operating at the BEPCII storage ring, we measure the cross sections of the $e^+e^- \to \pi^+\pi^- D^+D^-$ process at center-of-mass energies from 4.190 to 4.946 GeV with a partial reconstruction method. Resonance structures are seen and the cross section line shape can be described by the coherent sum of either two Breit-Wigner functions or a Breit-Wigner function and a phase space term. The mass and width of the resonance at about 4.4 GeV are determined to be $(4371.6 \pm 2.5 \pm 9.2)$ MeV/c^2 and $(167 \pm 4 \pm 29)$ MeV, respectively, which are in agreement with those of the $\psi(4360)$ or $Y(4390)$ state. The spin-3D-wave charmonium state $X(3842)$ is searched for through the $e^+e^- \to \pi^+\pi^- X(3842) \to \pi^+\pi^- D^+D^-$ process, and evidence with a significance of 4.2σ is found in the data samples with center-of-mass energies from 4.6 to 4.7 GeV.

DOI: 10.1103/PhysRevD.106.052012

I. INTRODUCTION

The charmonium states with masses below the open charm threshold and a few vector states above the open charm threshold are well established [1], and they agree well with theoretical calculations based on QCD [2–4] and QCD-inspired potential models [5–7]. The vector charmonia $\psi(4040)$, $\psi(4160)$, and $\psi(4415)$ were assigned as the 3^3S_1, 2^3D_1, and 4^3S_1 states, respectively, since only these three structures were observed in the total e^+e^- annihilation cross section [8].

However, a few more vector states, the Y states, were discovered by the *BABAR* and Belle B-factory experiments [9]. These include the $Y(4260)$ [10], the $Y(4360)$ [11,12], and the $Y(4660)$ [12]. They are produced via the initial state radiation (ISR) process in e^+e^- annihilation and, thus, are vector states with quantum numbers $J^{PC} = 1^{--}$, the same as the excited ψ states listed above. These states were observed in hidden-charm final states in contrast to the excited ψ states peaking in the inclusive hadronic cross section [8,13]. The final states in the latter are dominated by open-charm meson pairs.

In potential models, five vector charmonium states with masses between 4.0 and 4.7 GeV/c^2 are expected, namely the $\psi(3^3S_1)$, $\psi(2^3D_1)$, $\psi(4^3S_1)$, $\psi(3^3D_1)$, and $\psi(5^3S_1)$. The first three are often identified as the $\psi(4040)$, $\psi(4160)$, and $\psi(4415)$ states, respectively. The masses of the as yet undiscovered $\psi(3D)$ and $\psi(5S)$ are expected to be higher than 4.4 GeV/c^2. However, six vector states have been identified in the mass region between 4.0 and 4.7 GeV/c^2, as listed above. This makes the $Y(4260)$, the $Y(4360)$, and perhaps the $Y(4660)$ states good candidates for new types of exotic particles, and has stimulated theoretical work regarding their interpretation. They have been variously considered as candidates for tetraquark states, molecular states, hybrid states, and hadrocharmonia [3,14–16].

With masses above the open-charm thresholds, both Y and excited ψ states should couple to open-charm final states, and many studies have been performed to measure the cross sections of two-body final states with a pair of charmed mesons [17–20] and three-body final states with a pair of charmed mesons and a light meson [21]. Although four-body final states with a pair of charmed mesons and a pair of light mesons [22,23] have also been studied, and the production of intermediate two-body $[D_1(2420)\bar{D} + \text{c.c.}]$ and three-body $[\pi^+\pi^-\psi(3770)]$ states have been observed, the total cross section of the four-body final states has not been reported. In such final states, new exotic particles and new decay modes of known Y and excited ψ states can be searched for.

In this paper, we report the first measurement of the cross sections of the $e^+e^- \to \pi^+\pi^- D^+D^-$ process with the data samples taken at 37 center-of-mass energies ($\sqrt{s}$) from 4.190 to 4.946 GeV and the study of the decays of the excited ψ and Y states into this final state.

Two of the D-wave spin-triplet states $\psi(1^3D_1)$ ($\psi(3770)$) and $\psi(1^3D_2)$ ($\psi_2(3823)$) have been observed in the e^+e^- annihilation process $e^+e^- \to \pi^+\pi^-\psi(1D)$ [22–24]. As their spin partner, the $\psi(1^3D_3)$ ($X(3842)$) observed by LHCb [25] can also be produced in a similar process and can be searched for in the $\pi^+\pi^- D^+D^-$ final state, since the $X(3842)$ decays to $D\bar{D}$.

II. DETECTOR AND DATA SAMPLES

The BESIII detector [26] records e^+e^- collisions provided by the BEPCII storage ring [27]. The cylindrical core of the BESIII detector covers 93% of the full solid angle and consists of a helium-based multilayer drift chamber (MDC), a plastic scintillator time-of-flight (TOF) system, and a CsI(Tl) electromagnetic calorimeter (EMC), which are all enclosed in a superconducting solenoidal magnet providing a 1.0 T magnetic field. The solenoid is supported by an octagonal flux-return yoke with resistive plate counter muon identification modules interleaved with steel. The charged-particle momentum resolution at 1 GeV/c is 0.5%, and the dE/dx resolution is 6% for electrons from Bhabha scattering. The EMC measures photon energies

with a resolution of 2.5% (5%) at 1 GeV in the barrel (end cap) region. The time resolution in the TOF barrel region is 68 ps, while that in the end cap region is 110 ps. The end cap TOF system was upgraded in 2015 using multigap resistive plate chamber technology, providing a time resolution of 60 ps [28].

In this analysis, the experimental data samples used are listed in Table I. The center-of-mass energy is measured using dimuon events with a precision of 0.8 MeV for data samples with $\sqrt{s}$ smaller than 4.610 GeV [29,30] and using $\Lambda_c^+\bar{\Lambda}_c^-$ events with a precision of 0.6 MeV for data samples with $\sqrt{s}$ larger than or equal to 4.610 GeV [31]. The integrated luminosity is determined by analyzing large angle Bhabha scattering events with an uncertainty of 1.0% [31–33]. The integrated luminosity of the total data sample is 17.4 fb^{-1}.

To increase signal yields, a partial reconstruction method is employed for the $e^+e^- \to \pi^+\pi^- D^+ D^-$ process. A D^+ meson is reconstructed via its high branching fraction (9.38%) decay mode, $D^+ \to K^-\pi^+\pi^+$, and an additional $\pi^+\pi^-$ pair is selected from the remaining charged tracks. The recoil mass of the $\pi^+\pi^- D^+$ system is used to identify the D^- meson. Unless explicitly mentioned, the inclusion of charge conjugate modes is implied throughout the context.

Simulated data samples produced with a GEANT4-based [34] Monte Carlo (MC) package, which includes the geometric description of the BESIII detector and the

TABLE I. Yields and cross sections results for the $e^+e^- \to \pi^+\pi^- D^+ D^-$ process at different center-of-mass energies. Here, σ is the cross section of the $e^+e^- \to \pi^+\pi^- D^+ D^-$ process, where the first uncertainties are statistical and the second systematic; $\mathcal{L}$, S, and $\sigma_{\rm ul}$ are the integrated luminosity, statistical significance, and upper limit of the cross section at 90% confidence level, respectively. $N_{\rm signal}$ and $N_{\rm sideband}$ are the number of $e^+e^- \to \pi^+\pi^- D^+ D^-$ events from fits to $RM(D^+\pi_d^+\pi_d^-)$ distributions in $M(K^-\pi^+\pi^+)$ signal and sideband regions, respectively.

$\sqrt{s}$ nominal value (GeV)	$\sqrt{s}$ (MeV)	$\mathcal{L}$ (pb^{-1})	$N_{\rm signal}$	$N_{\rm sideband}$	σ (pb)	S	$\sigma_{\rm ul}$ (pb)
4.190	$4188.59 \pm 0.15 \pm 0.68$	570.0	-8 ± 10	-17 ± 11	$0.1 \pm 0.9 \pm 0.0$	⋯	1.0
4.200	$4199.15 \pm 0.05 \pm 0.34$	526.0	-5 ± 11	-15 ± 12	$0.2 \pm 1.0 \pm 0.0$	⋯	1.2
4.210	$4207.73 \pm 0.14 \pm 0.61$	572.1	15 ± 13	19 ± 14	$0.3 \pm 1.0 \pm 0.1$	1.2σ	2.6
4.220	$4217.13 \pm 0.14 \pm 0.67$	569.2	17 ± 12	14 ± 13	$0.7 \pm 0.9 \pm 0.1$	1.5σ	2.6
4.230	$4225.54 \pm 0.05 \pm 0.65$	1100.9	119 ± 25	12 ± 20	$3.4 \pm 0.8 \pm 0.3$	5.9σ	⋯
4.237	$4235.77 \pm 0.04 \pm 0.30$	530.3	25 ± 14	-29 ± 13	$2.6 \pm 1.0 \pm 0.2$	1.9σ	3.5
4.245	$4241.66 \pm 0.12 \pm 0.73$	55.9	5 ± 6	-3 ± 4	$4.0 \pm 3.7 \pm 0.3$	0.9σ	9.0
4.246	$4243.97 \pm 0.04 \pm 0.30$	538.1	101 ± 19	1 ± 15	$6.1 \pm 1.3 \pm 0.7$	6.6σ	⋯
4.260	$4258.00 \pm 0.06 \pm 0.60$	825.7	159 ± 26	17 ± 22	$5.6 \pm 1.1 \pm 0.5$	7.5σ	⋯
4.270	$4266.81 \pm 0.04 \pm 0.32$	531.1	61 ± 18	-27 ± 17	$4.3 \pm 1.2 \pm 0.4$	3.6σ	6.7
4.280	$4277.78 \pm 0.11 \pm 0.52$	175.7	25 ± 12	2 ± 11	$4.2 \pm 2.4 \pm 0.4$	2.2σ	9.0
4.290	$4288.43 \pm 0.06 \pm 0.34$	502.4	140 ± 23	4 ± 20	$8.6 \pm 1.6 \pm 0.7$	7.1σ	⋯
4.310	$4307.89 \pm 0.17 \pm 0.63$	45.1	25 ± 8	-4 ± 7	$17.1 \pm 5.5 \pm 1.5$	3.4σ	30
4.315	$4312.68 \pm 0.06 \pm 0.35$	501.2	263 ± 29	9 ± 23	$15.4 \pm 1.9 \pm 1.3$	11σ	⋯
4.340	$4337.93 \pm 0.06 \pm 0.35$	505.0	666 ± 42	20 ± 27	$36.9 \pm 2.5 \pm 3.1$	21σ	⋯
4.360	$4358.26 \pm 0.05 \pm 0.62$	544.0	1038 ± 53	8 ± 34	$48.2 \pm 2.6 \pm 4.1$	26σ	⋯
4.380	$4377.88 \pm 0.06 \pm 0.35$	522.7	1184 ± 67	-35 ± 37	$61.6 \pm 3.6 \pm 5.2$	25σ	⋯
4.390	$4387.40 \pm 0.17 \pm 0.65$	55.6	111 ± 18	19 ± 13	$46.2 \pm 8.8 \pm 3.9$	7.4σ	⋯
4.400	$4396.83 \pm 0.06 \pm 0.36$	507.8	1217 ± 62	61 ± 43	$61.9 \pm 3.5 \pm 5.2$	24σ	⋯
4.420	$4415.94 \pm 0.04 \pm 0.62$	1090.7	3144 ± 112	216 ± 71	$67.7 \pm 2.6 \pm 5.8$	37σ	⋯
4.440	$4437.59 \pm 0.06 \pm 0.35$	569.9	1588 ± 85	140 ± 59	$65.1 \pm 3.9 \pm 5.9$	23σ	⋯
4.470	$4467.06 \pm 0.11 \pm 0.73$	111.1	192 ± 35	36 ± 25	$36.0 \pm 7.8 \pm 3.9$	6.8σ	⋯
4.530	$4527.14 \pm 0.11 \pm 0.72$	112.1	141 ± 34	17 ± 28	$30.4 \pm 8.6 \pm 3.1$	4.1σ	41
4.575	$4574.50 \pm 0.18 \pm 0.70$	48.9	39 ± 18	12 ± 19	$15.5 \pm 9.9 \pm 1.4$	2.2σ	38
4.600	$4599.53 \pm 0.07 \pm 0.74$	586.9	811 ± 74	-16 ± 69	$31.2 \pm 3.1 \pm 2.8$	12σ	⋯
4.612	$4611.86 \pm 0.12 \pm 0.32$	103.8	139 ± 31	42 ± 29	$27.3 \pm 8.1 \pm 2.3$	4.9σ	40
4.620	$4628.00 \pm 0.06 \pm 0.32$	521.5	758 ± 90	30 ± 72	$33.7 \pm 4.4 \pm 2.9$	11σ	⋯
4.640	$4640.91 \pm 0.06 \pm 0.38$	552.4	725 ± 85	-65 ± 71	$32.2 \pm 3.9 \pm 2.8$	10σ	⋯
4.660	$4661.24 \pm 0.06 \pm 0.29$	529.6	814 ± 93	-51 ± 73	$38.1 \pm 4.6 \pm 3.4$	11σ	⋯
4.680	$4681.92 \pm 0.08 \pm 0.29$	1669.3	2427 ± 156	-12 ± 128	$33.7 \pm 2.3 \pm 2.8$	19σ	⋯
4.700	$4698.82 \pm 0.10 \pm 0.39$	536.5	1020 ± 85	-58 ± 76	$45.7 \pm 4.1 \pm 4.0$	13σ	⋯
4.740	$4739.70 \pm 0.20 \pm 0.30$	164.3	330 ± 45	47 ± 41	$39.8 \pm 6.5 \pm 3.4$	8.2σ	⋯
4.750	$4750.05 \pm 0.12 \pm 0.29$	367.2	781 ± 71	71 ± 59	$43.2 \pm 4.5 \pm 3.8$	13σ	⋯
4.780	$4780.54 \pm 0.12 \pm 0.33$	512.8	1042 ± 94	217 ± 78	$39.6 \pm 4.3 \pm 3.3$	14σ	⋯
4.840	$4843.07 \pm 0.20 \pm 0.31$	527.3	1050 ± 100	10 ± 81	$43.4 \pm 4.5 \pm 3.7$	13σ	⋯
4.914	$4918.02 \pm 0.34 \pm 0.35$	208.1	471 ± 67	40 ± 58	$48.6 \pm 7.9 \pm 4.2$	8.2σ	⋯
4.946	$4950.93 \pm 0.36 \pm 0.44$	160.4	247 ± 51	80 ± 51	$29.4 \pm 8.2 \pm 2.5$	5.0σ	⋯

detector response, are used to determine detection efficiencies and to estimate backgrounds. The simulation models the beam energy spread and ISR in the e^+e^- annihilations with the generator KKMC [35].

In order to estimate the potential background contributions, inclusive MC samples generated at $\sqrt{s} = 4.230$, 4.360, 4.420, and 4.600 GeV are used. The inclusive MC sample includes the production of open charm processes, the ISR production of vector charmonium(like) states, and the continuum processes incorporated in KKMC [35]. The known decay modes are modeled with EVTGEN [36] using branching fractions taken from the Particle Data Group (PDG) [1], and the remaining unknown charmonium decays are modeled with LUNDCHARM [37]. Final state radiation (FSR) from charged final state particles is incorporated using the PHOTOS package [38].

For the optimization of the selection criteria and signal extraction, the following MC samples are produced at each $\sqrt{s}$: $e^+e^- \to D_1(2420)^+D^-$, with $D_1(2420)^+ \to D^+\pi^+\pi^-$, $e^+e^- \to \pi^+\pi^-\psi(3770)$, with $\psi(3770) \to D^+D^-$, where $D_1(2420)^+D^-$ and $\pi^+\pi^-\psi(3770)$ are uniformly distributed in the phase space, and $e^+e^- \to \pi^+\pi^-D^+D^-$(PHSP) where the $\pi^+\pi^-D^+D^-$ events are uniformly distributed in the phase space to represent the processes with unknown intermediate states. For the $D_1(2420)^+ \to D^+\pi^+\pi^-$ process, the $D^+\pi^+\pi^-$ events are also uniformly distributed in the phase space.

III. EVENT SELECTION

Charged tracks detected in the MDC are required to be within a polar angle (θ) range of $|\cos\theta| < 0.93$, where θ is defined with respect to the z axis, which is the symmetry axis of the MDC. For charged tracks not originating from K^0_S or Λ decays, the distance of closest approach to the interaction point must be less than 10 cm along the z axis, $|V_z|$, and less than 1 cm in the transverse plane, $|V_{xy}|$.

Particle identification for charged tracks combines measurements of the energy loss (dE/dx) in the MDC and the flight time in the TOF. Likelihoods $\mathcal{L}(h)$ ($h = K, \pi, p$) for each hadron h hypothesis are formed, and each track is assigned to the particle type corresponding to the hypothesis with the highest likelihood. A proton (or an antiproton) is identified if $\mathcal{L}(p) > \mathcal{L}(\pi)$ and $\mathcal{L}(p) > \mathcal{L}(K)$. In order to suppress background from $e^+e^- \to \Lambda_c^+\bar{\Lambda}_c^-$ and other possible charmed baryons, events with proton or antiproton tracks are rejected. Charged kaons and pions are identified by comparing the likelihoods for the kaon and pion hypotheses, respectively.

To reconstruct the D^+ meson, one K^- and two π^+ candidate tracks are selected. They are required to originate from a common vertex and the quality of the vertex fit is required to satisfy $\chi^2_{VF} < 100$. All possible $K^-\pi^+\pi^+$ combinations in the event which satisfy these criteria are kept as D^+ candidates for further analysis. There are 1.1 D^+ candidates per event on average after $M(K^-\pi^+\pi^+)$ and $RM(D^+\pi_d^+\pi_d^-)$ requirements mentioned in the following paragraph. For each D^+ candidate, a $\pi^+\pi^-$ pair is selected from the charged tracks not used in D^+ reconstruction (referred to as π_d^+ and π_d^-) and the recoil mass of $D^+\pi_d^+\pi_d^-$ ($RM(D^+\pi_d^+\pi_d^-)$) is calculated to identify the D^- candidate.

Figure 1 shows $RM(D^+\pi_d^+\pi_d^-)$ versus the invariant mass of the $K^-\pi^+\pi^+$ ($M(K^-\pi^+\pi^+)$) for data samples at $\sqrt{s} = 4.230$, 4.420, and 4.680 GeV. Clear D^- and D^+ signal peaks can be seen in the $RM(D^+\pi_d^+\pi_d^-)$ and $M(K^-\pi^+\pi^+)$ distributions, respectively. The $\pi^+\pi^-D^+D^-$ signal region is defined as $|M(K^-\pi^+\pi^+) - m_{D^+}| < d_M$ and $|RM(D^+\pi_d^+\pi_d^-) - m_{D^-}| < d_{RM}$, and the sideband regions as $3d_M < |M(K^-\pi^+\pi^+) - m_{D^+}| < 5d_M$, and $3d_{RM} < |RM(D^+\pi_d^+\pi_d^-) - m_{D^-}| < 5d_{RM}$, where $m_{D^\pm} = 1.86966$ GeV/c^2 is the known $D^\pm$ mass [1]. The signal and sideband regions are indicated in Fig. 1. A linear mass or recoil mass dependence is assumed in estimating the background level in the signal region. The widths of the window are $d_M = 11$ MeV/c^2 for all the data samples, and $d_{RM} = 6$ MeV/c^2 for data samples with $\sqrt{s}$ smaller than 4.310 GeV, and $d_{RM} = 9$ MeV/c^2 for data samples with $\sqrt{s}$ greater than or equal to 4.310 GeV. Each sideband has the same width as that of the signal region.

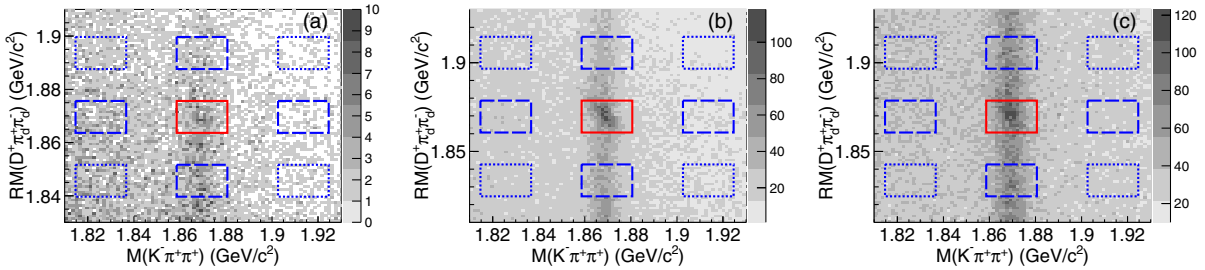

FIG. 1. Distributions of $RM(D^+\pi_d^+\pi_d^-)$ versus $M(K^-\pi^+\pi^+)$ for data samples at $\sqrt{s} = 4.230$ (a), 4.420 (b), and 4.680 (c) GeV. The red solid box shows the signal region, the blue dashed boxes the sideband regions with one real D^+ or D^- candidate, and the blue dotted boxes the sideband regions with fake D^+ and D^- candidates. The indices of the boxes from top to bottom and left to right are $(-1, 1)$, $(0, 1)$, $(1, 1)$, $(-1, 0)$, $(0, 0)$, $(1, 0)$, $(-1, -1)$, $(0, -1)$, and $(1, -1)$, respectively. The region with index $(0, 0)$ is the signal region, while the others are the sideband regions.

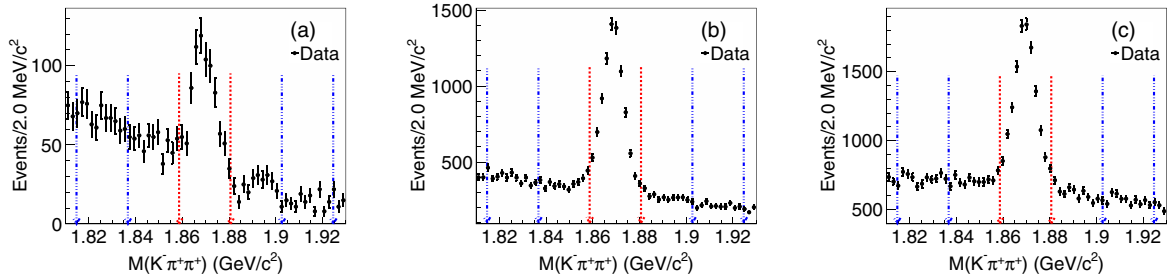

FIG. 2. The $K^-\pi^+\pi^+$ invariant mass distributions for data samples at $\sqrt{s} = 4.230$ (a), 4.420 (b), and 4.680 (c) GeV. The black dots with error bars are data, the regions between the two red dashed arrows are D^+ signal regions and those between blue dash-dotted arrows are sideband regions.

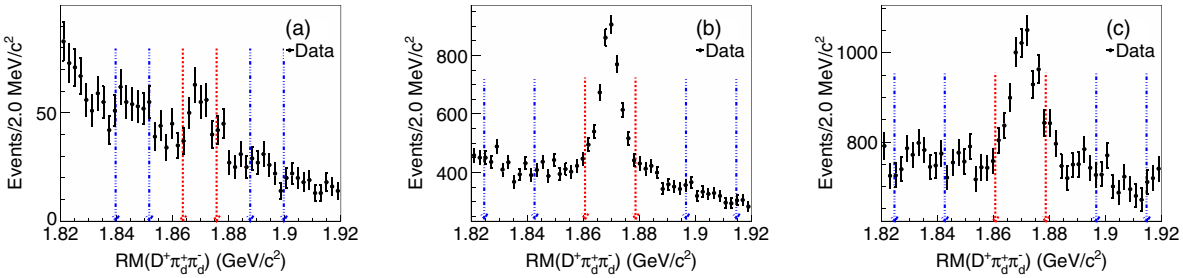

FIG. 3. Distributions of $RM(D^+\pi_d^+\pi_d^-)$ in the $M(K^-\pi^+\pi^+)$ signal region for data samples at $\sqrt{s} = 4.230$ (a), 4.420 (b), and 4.680 (c) GeV. The black dots with error bars are data, the regions between the two red dashed arrows are D^- signal regions and those between blue dash-dotted arrows are sideband regions.

After requiring $|RM(D^+\pi_d^+\pi_d^-) - m_{D^-}| < d_{RM}$, the $M(K^-\pi^+\pi^+)$ distributions are shown in Fig. 2 for data samples at $\sqrt{s} = 4.230$, 4.420, and 4.680 GeV as examples. In the following analysis, the $K^-\pi^+\pi^+$ combination in the signal region is constrained to the known D^+ mass, m_{D^+} in the PDG [1], with a kinematic fit to improve its momentum resolution, and those in the sideband regions are constrained to the central value of the corresponding sideband region.

Figure 3 shows the $RM(D^+\pi_d^+\pi_d^-)$ distributions after requiring $|M(K^-\pi^+\pi^+) - m_{D^+}| < d_M$ for data samples at $\sqrt{s} = 4.230$, 4.420, and 4.680 GeV. Clear D^- signal peaks are visible in all data samples. The D^- signal and sideband regions are indicated by the arrows.

The $e^+e^- \to D^0D^-\pi^+$ process produces a peaking background in the $RM(D^+\pi_d^+\pi_d^-)$ distribution as shown in Fig. 4(a). The peaking background may come from $e^+e^- \to D^0D^-\pi^+$, with $D^0 \to K^-\pi_d^+\pi_d^-\pi^+$, where a directly produced π^+, together with π^+ and K^- from D^0, forms the tagged D^+. Figure 4(b) shows the $M(K^-\pi_d^+\pi_d^-\pi^+)$[1] distribution, where a clear D^0 peak is seen. We require $|M(K^-\pi_d^+\pi_d^-\pi^+) - m_{D^0}| > 0.01$ GeV/c^2 to veto these D^0 background contributions, where $m_{D^0} = 1.86484$ GeV/c^2 [1]. The value of 0.01 GeV/c^2 corresponds to about twice the resolution of $M(K^-\pi_d^+\pi_d^-\pi^+)$, which is 0.0045 GeV/$c^2$. The effectiveness of this veto can be seen in Fig. 4(c). The number of $e^+e^- \to \pi^+\pi^-D^+D^-$ events from fits to the $RM(D^+\pi_d^+\pi_d^-)$ distributions in the $M(K^-\pi^+\pi^+)$ sideband region before and after the veto are 614 ± 92 and 216 ± 72, respectively.

After applying all the above selection criteria, we compare distributions for events in the D^+ and D^- signal region (S sample) and sideband regions (B sample) to further suppress non-$\pi^+\pi^-D^+D^-$ background. The B sample is defined as

$$B = f_1 \cdot (B_{-1,0} + B_{1,0}) + f_2 \cdot (B_{0,-1} + B_{0,1}) - f_3 \cdot (B_{-1,-1} + B_{1,-1} + B_{-1,1} + B_{1,1}), \quad (1)$$

where $B_{i,j}$ is the sideband region defined in Fig. 1, $f_1 = 0.5$, $f_2 = 0.5$, and $f_3 = f_1 f_2 = 0.25$ are the normalization factors assuming a linear mass dependence in the background distributions. In order to improve the momentum resolutions of the final state particles, the $RM(D^+\pi_d^+\pi_d^-)$ combination in the signal region is constrained to the known D^- mass, m_{D^-} in the PDG [1], and a total four-momentum conservation constraint to that of the initial e^+e^- system are applied. For events in the $RM(D^+\pi_d^+\pi_d^-)$ sidebands, the recoiling mass of the $D^+\pi_d^+\pi_d^-$ combination is constrained to the central value of the corresponding sideband region.

[1]Here, π^+ could be either of the charged pions in the decay $D^+ \to K^-\pi^+\pi^+$.

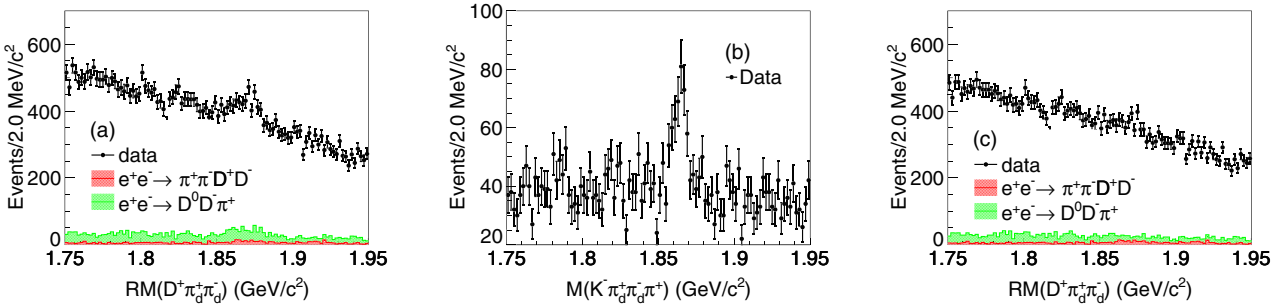

FIG. 4. The $RM(D^+\pi_d^+\pi_d^-)$ distribution for combinations in the $M(K^-\pi^+\pi^+)$ sideband before (a) and after (c) the D^0 veto at $\sqrt{s} = 4.420$ GeV. The $M(K^-\pi_d^+\pi_d^-\pi^+)$ distribution in the $M(K^-\pi^+\pi^+)$ signal region is shown in the middle plot (b). The black dots with error bars are data and the red and green histograms are MC simulations of $e^+e^- \to \pi^+\pi^- D^+D^-$(PHSP) and $e^+e^- \to D^0D^-\pi^+$ processes, respectively, with inclusive decays of both D mesons. The normalizations of $e^+e^- \to \pi^+\pi^- D^+D^-$(PHSP) and $e^+e^- \to D^0D^-\pi^+$ processes are according to cross sections of total $e^+e^- \to \pi^+\pi^- D^+D^-$ process and $e^+e^- \to D^0D^-\pi^+$ process measured from data samples, respectively.

The invariant mass distribution of the $\pi_d^+\pi_d^-$ pair is shown in Fig. 5(a), where clear K_S^0 peaks can be seen in both the S and B samples. In order to veto the $K_S^0 \to \pi_d^+\pi_d^-$ background, a secondary vertex fit is performed on the $\pi_d^+\pi_d^-$ pair. The decay length $L_{\pi_d^+\pi_d^-}$ divided by its uncertainty $\Delta_{L_{\pi_d^+\pi_d^-}}$ of the combinations with $\pi_d^+\pi_d^-$ invariant mass between 491.0 and 503.5 MeV/c^2 is shown in Fig. 5(b). By requiring $|L_{\pi_d^+\pi_d^-}/\Delta_{L_{\pi_d^+\pi_d^-}}| < 2$ the K_S^0 background is suppressed significantly as shown in Fig. 5(c).

The $|V_{xy}|$ and $|V_z|$ distributions of the K^- and π^+ tracks used in D^+ tag, and the π_d^+ and π_d^- tracks from direct e^+e^- annihilation are shown in Fig. 6. Compared with the typical requirements of less than 1 and 10 cm for $|V_{xy}|$ and $|V_z|$, respectively, a set of tighter selection criteria $|V_{xy}| <$ 0.55 cm and $|V_z| < 3$ cm is identified by optimizing the $\pi^+\pi^-D^+D^-$ signal significance.

After applying all the above selection criteria except the D^- mass constraint and the four-momentum conservation constraint, requiring $|M(K^-\pi^+\pi^+) - m_{D^+}| < d_M$, and constraining $M(K^-\pi^+\pi^+)$ to the D^+ mass, we obtain the $RM(D^+\pi_d^+\pi_d^-)$ distributions [Figs. 7(a),7(c),7(e)] for data samples at $\sqrt{s} = 4.230$, 4.420, and 4.680 GeV. The non-$\pi^+\pi^-D^+D^-$ background is studied by examining the $RM(D^+\pi_d^+\pi_d^-)$ distributions [Figs. 7(b),7(d),7(f)] for $K^-\pi^+\pi^+$ combinations in the D^+ mass sideband regions. No significant D^- signal peaks are observed in the sideband samples. The number of $e^+e^- \to \pi^+\pi^-D^+D^-$ signal events is obtained by subtracting the number of D^- signal candidates in the D^+ sideband regions from that in the D^+ signal region, as discussed in Sec. IV.

IV. CROSS SECTIONS OF THE $e^+e^- \to \pi^+\pi^-D^+D^-$ PROCESS

The cross section of the $e^+e^- \to \pi^+\pi^-D^+D^-$ process is calculated with

$$\sigma = \frac{N_{\rm signal} - N_{\rm sideband}/2}{2f(\sum_i \omega_i \epsilon_i (1+\delta)_i)\frac{1}{|1-\Pi|^2}\mathcal{B}\mathcal{L}}, \tag{2}$$

where $N_{\rm signal}$ and $N_{\rm sideband}$ are the number of $e^+e^- \to \pi^+\pi^-D^+D^-$ events from maximum-extended-likelihood fits to $RM(D^+\pi_d^+\pi_d^-)$ distributions (Fig. 7) in the $M(K^-\pi^+\pi^+)$ signal and sideband regions, respectively, $\frac{1}{|1-\Pi|^2}$ is the vacuum polarization factor, $\mathcal{B}$ is the branching fraction of the decay $D^+ \to K^-\pi^+\pi^+$ [1], and $\mathcal{L}$ is the integrated luminosity of the data sample. f denotes an efficiency correction factor

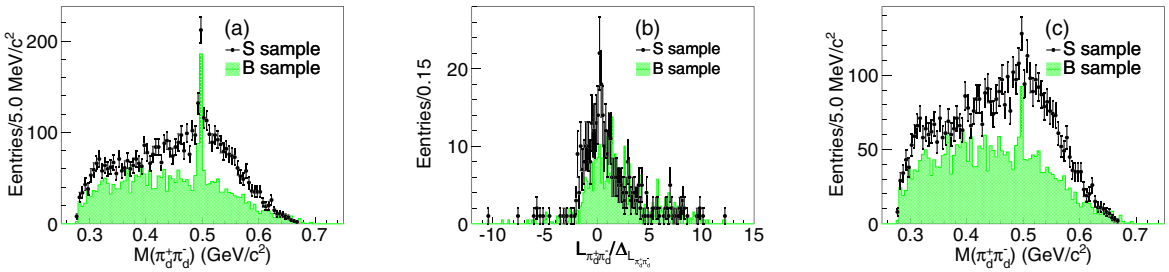

FIG. 5. Distributions of $M(\pi_d^+\pi_d^-)$ before (a) and after (c) the $|L_{\pi_d^+\pi_d^-}/\Delta_{L_{\pi_d^+\pi_d^-}}| < 2$ requirement, and the $L_{\pi_d^+\pi_d^-}/\Delta_{L_{\pi_d^+\pi_d^-}}$ distribution (b) at $\sqrt{s} = 4.420$ GeV. The black dots with error bars stand for the S sample and the green shaded histograms for the B sample.

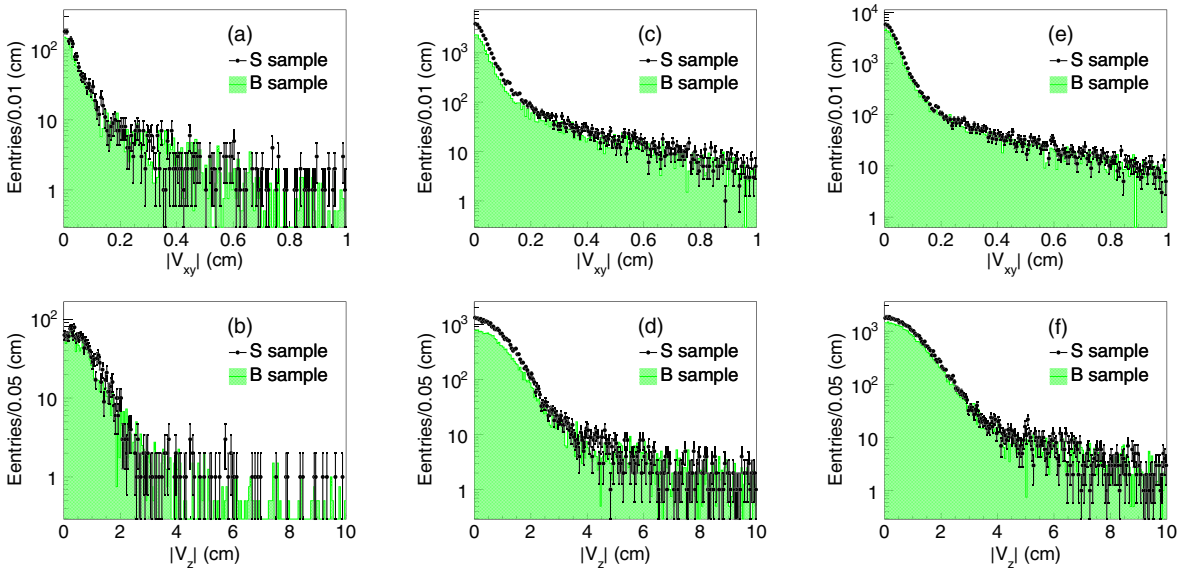

FIG. 6. Distributions of $|V_{xy}|$ for data samples at $\sqrt{s} = 4.230$ (a), 4.420 (c), and 4.680 (e) GeV, and those of $|V_z|$ for data samples at $\sqrt{s} = 4.230$ (b), 4.420 (d), and 4.680 (f) GeV. The black dots with error bars correspond to the S sample and the shaded histograms to the B sample.

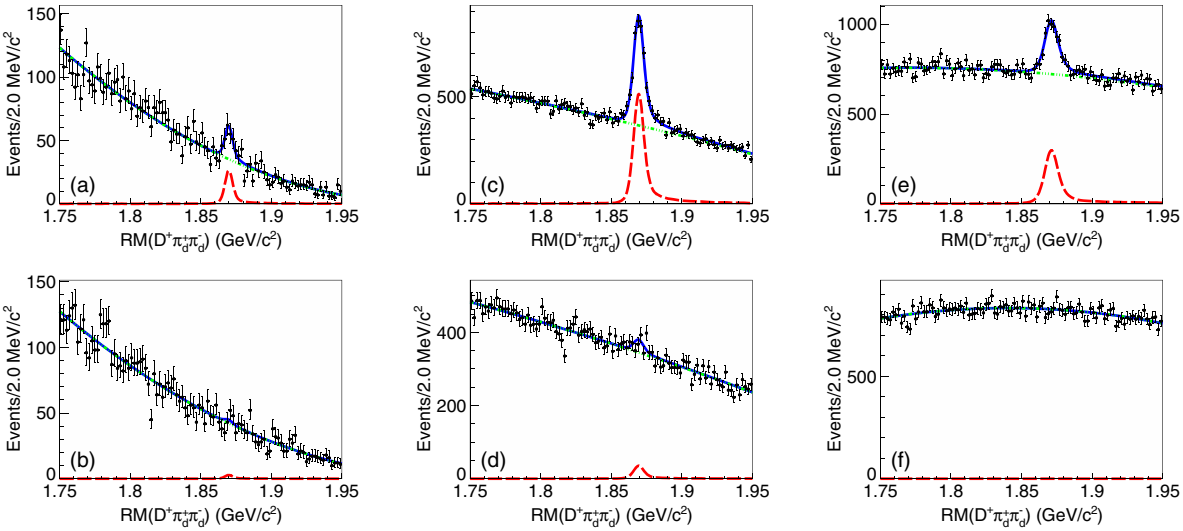

FIG. 7. Distributions of $RM(D^+\pi_d^+\pi_d^-)$ in $M(K^-\pi^+\pi^+)$ signal (a), (c), (e) and sideband (b), (d), (f) regions for data samples at $\sqrt{s} = 4.230$ (a), (b), 4.420 (c), (d), and 4.680 (e), (f) GeV, and the best fits to the distributions. The black dots with error bars are data, the red dashed, green dash-dotted, and blue solid lines are the signal, background, and total fit, respectively. The fit qualities are tested using a χ^2-test method, with $\chi^2/\text{n.d.f.} = 93.72/91$, 96.39/95, 83.74/93, 104.25/95, 98.69/93, and 85.12/95 for (a), (b), (c), (d), (e), and (f), respectively. The n. d. f. denotes the number of degrees of freedom.

$$f = f^{M(K^-\pi^+\pi^+)} f^{K\nrightarrow p} f^{V_{xy,z}} f^{L/\Delta_L} f^{RM(D^+\pi_d^+\pi_d^-)}, \qquad (3)$$

with f^v referring to the efficiency correction factor caused by selection criterion v, which includes $M(K^-\pi^+\pi^+)$ and $RM(D^+\pi_d^+\pi_d^-)$ mass window requirements, $p/\bar{p}$ veto ($K\nrightarrow p$), $V_{xy,z}$ requirements, and $L_{\pi_d^+\pi_d^-}/\Delta_{L_{\pi_d^+\pi_d^-}}$ requirement for K_S^0 background suppression. Details on the evaluation of f^v can be found in Sec. VII A. $(1+\delta)_i$ is the ISR correction factor, and ω_i and ϵ_i are the fraction and the detection efficiency of subprocess i, respectively, here, $i = 0$, 1, and 2 correspond to $e^+e^- \to D_1(2420)^+D^- \to \pi^+\pi^-D^+D^-$, $e^+e^- \to \pi^+\pi^-\psi(3770) \to \pi^+\pi^-D^+D^-$, and $e^+e^- \to \pi^+\pi^-D^+D^-(\text{PHSP})$ subprocess, respectively. ω_i is estimated from the S sample by a one-dimensional simultaneous extended-unbinned-likelihood fit to $RM(D^+)$, $RM(D^-_{\text{miss}})$, and $RM(\pi_d^+\pi_d^-)$ distributions,

TABLE II. The values for f and $\Sigma\omega_i\epsilon_i(1+\delta)_i$. Here, f is the efficiency correction factor, ϵ_i, $(1+\delta)_i$, and ω_i are the detection efficiency, ISR correction factor, and fraction of each subprocess i, respectively.

$\sqrt{s}^{\text{nominal}}$ (GeV)	f	$\Sigma\omega_i\epsilon_i(1+\delta)_i$	$\sqrt{s}^{\text{nominal}}$ (GeV)	f	$\Sigma\omega_i\epsilon_i(1+\delta)_i$
4.190	0.960	0.126	4.420	0.960	0.217
4.200	0.960	0.133	4.440	0.960	0.216
4.210	0.960	0.138	4.470	0.960	0.229
4.220	0.960	0.148	4.530	0.960	0.204
4.230	0.960	0.157	4.575	0.960	0.232
4.237	0.960	0.158	4.600	0.960	0.235
4.245	0.960	0.165	4.610	0.960	0.220
4.246	0.960	0.162	4.620	0.960	0.223
4.260	0.960	0.170	4.640	0.960	0.224
4.270	0.960	0.173	4.660	0.960	0.219
4.280	0.960	0.174	4.680	0.960	0.228
4.290	0.960	0.169	4.700	0.960	0.225
4.310	0.960	0.187	4.740	0.960	0.247
4.315	0.960	0.177	4.750	0.960	0.247
4.340	0.960	0.186	4.780	0.960	0.242
4.360	0.960	0.208	4.840	0.960	0.240
4.380	0.960	0.197	4.914	0.960	0.235
4.390	0.960	0.210	4.946	0.960	0.231
4.400	0.960	0.200	⋯	⋯	⋯

and the background is estimated by the B sample. For data samples with $\sqrt{s}$ larger than 4.315 GeV, $i=0$, 1, and 2, while for data samples with $\sqrt{s}$ smaller than or equal to 4.315 GeV, $i=1$ and 2, since the threshold of $D_1(2420)\bar{D}$ is 4291.75 MeV/c^2, and no significant $D_1(2420)\bar{D}$ events are observed at $\sqrt{s}=4.310$ and 4.315 GeV.

Figure 7 shows the fit results of data samples at $\sqrt{s}=4.230$, 4.420, and 4.680 GeV. The signal shape is modeled by the $RM(D^+\pi_d^+\pi_d^-)$ distributions in MC simulation of each subprocess weighted according to ω_i and convolved with a Gaussian function to take the resolution difference between data and MC simulation into account. The background shape is described by a second-order Chebychev polynomial function. At each $\sqrt{s}$, the signal shape for the fit in the $M(K^-\pi^+\pi^+)$ sideband regions is the same as that for the fit in the $M(K^-\pi^+\pi^+)$ signal region. The results for N_{signal} and N_{sideband} obtained from the fits are listed in Table I, together with the fit results for all other data samples. The values for f and $\Sigma\omega_i\epsilon_i(1+\delta)_i$ are listed in Table II. The calculated cross section of the $e^+e^-\to\pi^+\pi^-D^+D^-$ process is shown in Fig. 8.

For data samples where no significant $e^+e^-\to\pi^+\pi^-D^+D^-$ signal peaks are observed (statistical significance smaller than 5σ), the upper limits on the cross section are calculated using a Bayesian method [39]. By fitting the $RM(D^+\pi_d^+\pi_d^-)$ distribution for the events in the D^+ signal region with fixed values for the signal yield, a scan of the likelihood distribution as a function of the cross section is obtained. To take the total systematic uncertainty (listed in Table VII) into consideration, the likelihood distribution is convolved with a Gaussian function with a width corresponding to the overall systematic uncertainty. The upper limit on the cross section at 90% confidence level (CL) is obtained from $\int_0^\sigma L(x)dx/\int_0^\infty L(x)dx=0.9$. The upper limits on the cross sections are listed in Table I.

V. RESONANCES IN THE $e^+e^-\to\pi^+\pi^-D^+D^-$ CROSS SECTION LINE SHAPE

Resonant structures around $\sqrt{s}=4.4$ and 4.7 GeV can be seen in Fig. 8, and there is no significant signal at other energies, such as the $\psi(4230)$. Least-square fits to the measured $e^+e^-\to\pi^+\pi^-D^+D^-$ cross sections are performed to study the resonance structures. The χ^2 is constructed as

$$\chi^2=\sum_i\frac{(\sigma_i-\sigma_i^{\text{fit}})^2}{\delta_i^2},$$

where σ_i and σ_i^{fit} are the measured and fitted cross sections of the ith data sample, respectively, and δ_i is the statistical uncertainty of the measured cross section.

The cross sections are described with one Breit-Wigner (BW) function,

$$\sigma(\sqrt{s})=|BW_0(\sqrt{s})|^2, \tag{4}$$

a coherent sum of two BW functions,

$$\sigma(\sqrt{s})=|BW_0(\sqrt{s})+BW_1(\sqrt{s})e^{i\phi_1}|^2, \tag{5}$$

a coherent sum of one BW function and a phase space term,

$$\sigma(\sqrt{s})=|BW_0(\sqrt{s})+ce^{i\phi_2}\Phi_4(\sqrt{s})|^2, \tag{6}$$

and a coherent sum of two BW functions and a phase space term,

$$\sigma(\sqrt{s})=|BW_0(\sqrt{s})+BW_1(\sqrt{s})e^{i\phi_1}+ce^{i\phi_2}\Phi_4(\sqrt{s})|^2, \tag{7}$$

respectively. The BW function is defined as

$$BW_j(\sqrt{s})=\frac{\sqrt{12\pi\Gamma_j^{e^+e^-}\Gamma_j^{\text{tot}}\mathcal{B}_j}}{s-m_j^2+im_j\Gamma_j^{\text{tot}}}\sqrt{\frac{\Phi_4(\sqrt{s})}{\Phi_4(m_j)}}, \tag{8}$$

where m_j, Γ_j^{tot}, and $\Gamma_j^{e^+e^-}$ are the mass, width, and electronic partial width of the jth resonance (R_j), respectively; $\mathcal{B}_j$ is the branching fraction of the decay $R_j\to\pi^+\pi^-D^+D^-$, ϕ_j is the relative phase between the jth resonance as well as the phase space term, $\Phi_4(\sqrt{s})$ is the phase space factor of the four-body decay

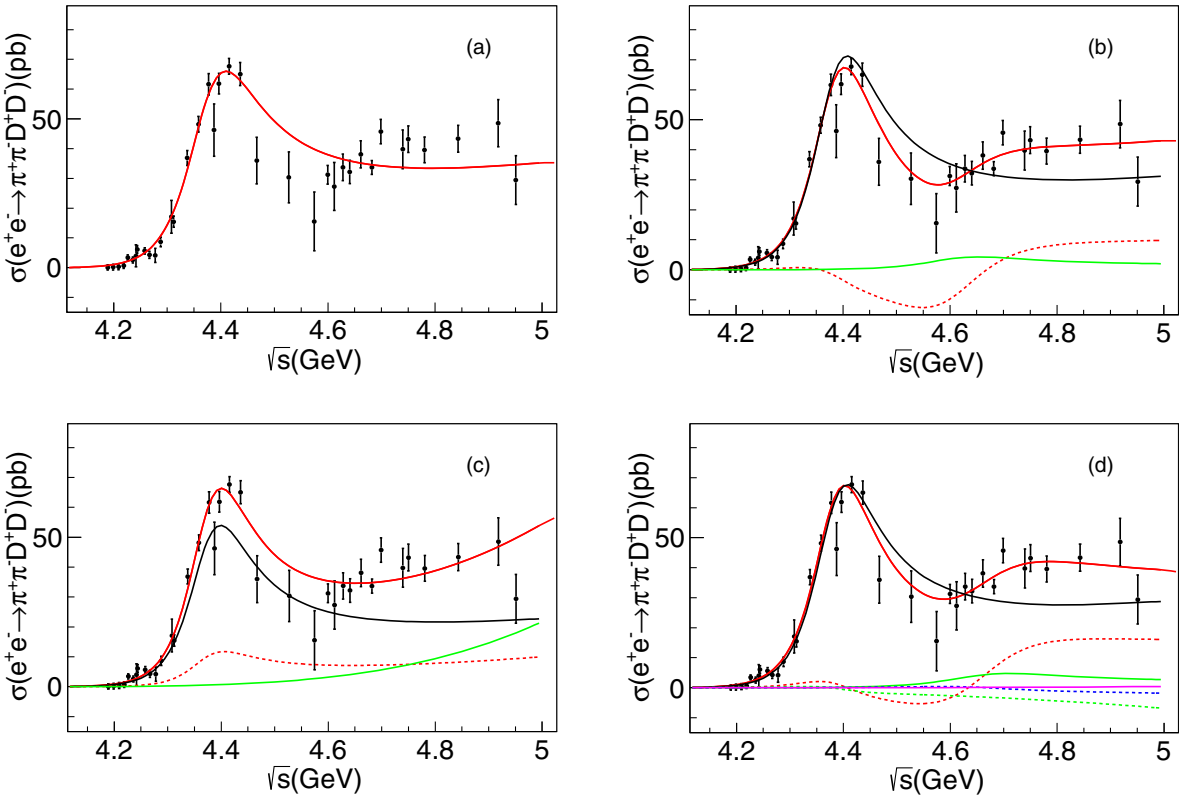

FIG. 8. Cross section of the process $e^+e^- \to \pi^+\pi^- D^+ D^-$ and fits with Eq. (4) (a), with Eq. (5) (solution II) (b), with Eq. (6) (solution I) (c), and with Eq. (7) (solution I) (d). Other solutions of fits with Eqs. (5), (6), and (7) are shown in Tables III, IV, and V, respectively. Dots with error bars are data with the statistical uncertainties and the red solid lines show the best fit results. For (b), the black and green solid lines describe R_0 and R_1 components, respectively, and the red dashed line describes the interference between them; for (c), the black and green solid lines describe R_0 and Φ_4 components, respectively, and the red dashed line describes the interference between them; and for (d), the black, green, and pink solid lines describe R_0, R_1, and Φ_4 components, respectively, and the red, green, and blue dashed lines describe the interference between R_0 and R_1, R_0 and Φ_4, and R_1 and Φ_4, respectively.

$R \to \pi^+\pi^- D^+ D^-$, and c is a constant describing the magnitude of $\Phi_4(\sqrt{s})$.

The fit with a single resonance [Fig. 8(a)] results in a $\chi^2/\text{n.d.f.} = 77.8/34$, corresponding to a CL of 2.8×10^{-5}. This indicates that using R_0 only cannot describe the cross section line shape well. Adding another BW function or a four-body phase space term improves the fit quality to an acceptable level of $\chi^2/\text{n.d.f.} = 46.1/30$ (CL = 3.0%) or 59.9/32 (CL = 0.2%), respectively. The fits are shown in Figs. 8(b) and 8(c), respectively, and the statistical significance of the second resonance or the four-body phase space term is found to be 4.7σ and 3.8σ, respectively. The fit with both a second resonance and a four-body phase space term shown in Fig. 8(d) improves the fit very little ($\Delta\chi^2 = 0.2$) compared with the fit with two resonances but improves relatively large ($\Delta\chi^2 = 14.0$) compared with that with the coherent sum of a resonance and a four-body phase space term. From these we conclude that we observe a resonance at around 4.4 GeV and evidence for either another resonance at 4.7 GeV or a nonresonant amplitude described with a four-body phase space or the combination of both of them.

The resonance parameters for R_0 obtained by fitting with Eq. (4) are $m_0 = (4371.6 \pm 2.5)$ MeV/c^2, $\Gamma_0^{\text{tot}} = (166.8 \pm 4.2)$ MeV, and $\Gamma_0^{e^+e^-}\mathcal{B}_0 = (12.0 \pm 0.3)$ eV; whereas those from fits with other scenarios are listed in Tables III, IV, and V. There are multiple solutions in the latter cases where the masses and widths are identical but the amplitudes and the relative phases are different in different solutions, as can be seen from the tables. The resonance parameters for R_0 obtained by fitting with Eq. (4) are taken as the nominal results and the difference from those obtained by adding R_1, or Φ_4, or both of them are taken as the systematic uncertainties as discussed later in Sec. VII B.

Other than the R_0 and R_1 contributions, we also test the statistical significances of the possible structures around $\sqrt{s} = 4.230$ and 4.914 GeV. By adding the $\psi(4230)$ amplitude to the fit, with the mass and width fixed according to the world averaged values [1], its significance is found to be only 0.9σ. By adding a new resonance at high energy with free mass and width, the statistical significance is found to be 0.6σ.

Note that there are three points ($\sqrt{s}$ from 4.4 to 4.6 GeV) systematically below the fitted line. Since the integrated

TABLE III. The fitted parameters of the cross sections of $e^+e^- \to \pi^+\pi^- D^+ D^-$ with Eq. (5). The uncertainties are statistical only.

Parameters	Solution 1	Solution 2
$m_0(\mathrm{MeV}/c^2)$	4378.0 ± 6.2	
Γ_0^{tot} (MeV)	152 ± 12	
$m_1(\mathrm{MeV}/c^2)$	4604 ± 135	
Γ_1^{tot} (MeV)	245 ± 61	
$\Gamma_0^{e^+e^-}\mathcal{B}_0$ (eV)	21 ± 12	12.2 ± 5.8
$\Gamma_1^{e^+e^-}\mathcal{B}_1$ (eV)	54 ± 15	1.3 ± 2.7
ϕ_1 (rad)	4.1 ± 0.3	5.6 ± 2.6

TABLE IV. The fitted parameters of the cross sections of $e^+e^- \to \pi^+\pi^- D^+ D^-$ with Eq. (6). The uncertainties are statistical only.

Parameters	Solution 1	Solution 2
$c(\mathrm{MeV}^{-3/2})$	57 ± 19	
$m_0(\mathrm{MeV}/c^2)$	4371.1 ± 3.4	
Γ_0^{tot} (MeV)	144.5 ± 6.9	
$\Gamma_0^{e^+e^-}\mathcal{B}_0$ (eV)	8.9 ± 0.6	12.9 ± 1.3
ϕ_2 (rad)	1.7 ± 0.3	1.5 ± 0.2

TABLE V. The fitted parameters of the cross sections of $e^+e^- \to \pi^+\pi^- D^+ D^-$ with Eq. (7). The uncertainties are statistical only.

Parameters	Solution 1	Solution 2	Solution 3	Solution 4
$c(\mathrm{MeV}^{-3/2})$	8 ± 16			
$m_0(\mathrm{MeV}/c^2)$	4378.2 ± 5.5			
Γ_0^{tot} (MeV)	148.9 ± 9.0			
$m_1(\mathrm{MeV}/c^2)$	4649 ± 95			
Γ_1^{tot} (MeV)	282 ± 185			
$\Gamma_0^{e^+e^-}\mathcal{B}_0$ (eV)	11.5 ± 2.3	11.5 ± 2.3	19.1 ± 6.0	19.4 ± 5.6
$\Gamma_1^{e^+e^-}\mathcal{B}_1$ (eV)	1.6 ± 1.7	1.7 ± 1.9	59 ± 23	61 ± 22
ϕ_1 (rad)	6.1 ± 1.1	6.1 ± 1.1	4.2 ± 0.4	4.2 ± 0.3
ϕ_2 (rad)	2.5 ± 2.2	6.2 ± 7.4	5.3 ± 6.8	5.3 ± 5.6

luminosities of these data samples are low, larger data samples are desired to confirm the above conclusions.

VI. EVIDENCE FOR $e^+e^- \to \pi^+\pi^- X(3842)$

To search for the $X(3842)$ state, the S sample defined in Sec. III with the additional K_S^0 veto and stringent $|V_{xy}|$ and $|V_z|$ requirements is used. In order to suppress the $e^+e^- \to D_1(2420)^+ D^-$ background, the $D_1(2420)$ signal is suppressed by requiring $|RM(D^+) - m_{D_1(2420)^-}| > 0.01\,\mathrm{GeV}/c^2$ and $|RM(D^-_{\mathrm{miss}}) - m_{D_1(2420)^+}| > 0.01\ \mathrm{GeV}/c^2$, where $m_{D_1(2420)^\pm} = 2.4221\ \mathrm{GeV}/c^2$ is the known $D_1(2420)^\pm$ mass [1].

The $RM(\pi_d^+\pi_d^-)$ (equivalent to the invariant mass of $D^+ D^-_{\mathrm{miss}}$) distributions in all data samples are examined. While no significant signal is observed at any single $\sqrt{s}$, there is evidence for an $X(3842)$ resonance for $\sqrt{s}$ from 4.600 to 4.700 GeV. Figure 9 shows the $RM(\pi_d^+\pi_d^-)$ distributions at $\sqrt{s} = 4.420$, 4.680 GeV, and data samples with $\sqrt{s}$ from 4.600 to 4.700 GeV.

A maximum-extended-likelihood fit to the $RM(\pi_d^+\pi_d^-)$ distribution is performed. The $X(3842)$ signal shape is obtained from MC simulation of the $e^+e^- \to f_0(500)X(3842) \to \pi^+\pi^- D^+ D^-$ process, and convolved with a Gaussian function to take the resolution difference between data and MC simulation into account. The mean and sigma values of the Gaussian function for other fits are fixed to the fit values obtained at $\sqrt{s} = 4.680$ GeV as this sample contains the largest number of signal events. The mass and width of the $f_0(500)$ are taken from Ref. [40] when generating MC events. The background is described with a second-order Chebychev polynomial function.

Fit results of the $RM(\pi_d^+\pi_d^-)$ distributions are shown in Figs. 9(a)–9(c). The signal yields (statistical significances) are -39 ± 18 (2.0σ), 58 ± 24 (1.8σ), and 155 ± 38 (4.2σ) at $\sqrt{s} = 4.420$, 4.680 GeV and data samples with $\sqrt{s}$ from 4.600 to 4.700 GeV, respectively. Furthermore, for data samples with $\sqrt{s}$ from 4.600 to 4.700 GeV, the fits are also performed by changing the fit range, the signal shape, or the background shape. In all cases, the minimum value of the $X(3842)$ resonance significance is 4.2σ. The fit results at other energies are listed in Table VI. The cross sections of the $e^+e^- \to \pi^+\pi^- X(3842) \to \pi^+\pi^- D^+ D^-$ process are calculated with

$$\sigma = \frac{N}{2\mathcal{B}\epsilon_X \mathcal{L}(1+\delta)_X \frac{1}{|1-\Pi|^2}}, \tag{9}$$

where N is the number of $e^+e^- \to \pi^+\pi^- D^+ D^-$ events from fits to $RM(\pi_d^+\pi_d^-)$ distributions (Fig. 9), and ϵ_X and $(1+\delta)_X$ are the detection efficiency and ISR correction factor of $e^+e^- \to f_0(500)X(3842) \to \pi^+\pi^- D^+ D^-$ process. The upper limits of the cross sections are determined using a similar strategy to that described in Sec. IV. The results are also listed in Table VI.

VII. SYSTEMATIC UNCERTAINTIES

A. Systematic uncertainties for the $e^+e^- \to \pi^+\pi^- D^+ D^-$ cross sections

The systematic uncertainties in the cross section measurement of the $e^+e^- \to \pi^+\pi^- D^+ D^-$ process stem from many sources. The systematic uncertainties associated with the detection efficiencies, including tracking and particle identification [41], are estimated as 1% for each track. The systematic uncertainty associated with the integrated luminosity measurement using Bhabha ($e^+e^- \to e^+e^-$) events is estimated as 1% [42]. For the vacuum polarization factor

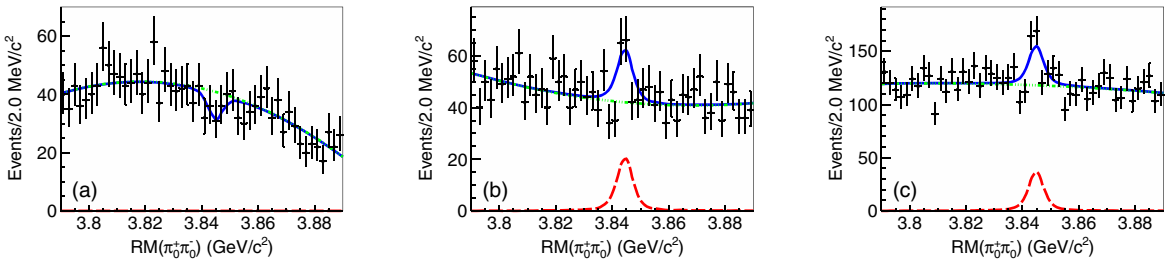

FIG. 9. The $RM(\pi_d^+\pi_d^-)$ distributions and the fits at $\sqrt{s} = 4.420$ (a), 4.680 (b) GeV, and data samples with $\sqrt{s}$ from 4.600 to 4.700 GeV (c). The black dots with error bars are the S sample, and the red dashed, green dash-dotted, and blue solid curves are the signal shape, background shape, and total fit, respectively. The fit qualities are tested using a χ^2-test method, with $\chi^2/\text{n.d.f.} = 26.3/45$, 41.4/43, and 57.07/45 for (a), (b), and (c), respectively.

calculation, the systematic uncertainty originates mainly from hadronic contributions, and is estimated as 0.1% according to Ref. [43]. The systematic uncertainty coming from the input branching fraction of $D^+ \to K^-\pi^+\pi^+$ is estimated as 1.7% [1]. Details of further systematic uncertainties are given below.

The selection efficiency is obtained from MC simulation and corrected according to the measurements with control samples selected from data directly. The efficiency correction factor f^v is defined as

$$f^v = \epsilon^v_{\text{data}}/\epsilon^v_{\text{MC}}, \tag{10}$$

with

$$\epsilon^v_{\text{data(MC)}} = N^v_{\text{signal}_{\text{data(MC)}}}/N^v_{\text{all}_{\text{data(MC)}}}, \tag{11}$$

TABLE VI. Results for the $e^+e^- \to \pi^+\pi^- X(3842) \to \pi^+\pi^- D^+D^-$ process. Here, σ is the cross section of the $e^+e^- \to \pi^+\pi^- X(3842) \to \pi^+\pi^- D^+D^-$ process, where the first uncertainty is statistical and the second systematic; S is the statistical significance; ϵ_X, $(1+\delta)_X$, N, and σ_{ul} are the detection efficiency, ISR correction factor, signal yields, and the upper limit of cross section at 90% confidence level.

$\sqrt{s}^{\text{nominal}}$	$\epsilon_X(\%)$	$(1+\delta)_X$	$\mathcal{L}$ (pb^{-1})	N	σ (pb)	S	σ_{ul} (pb)
4.190	3.29	0.804	570.0	1 ± 2	$0.5 \pm 0.8 \pm 0.1$	0.6σ	2.5
4.200	4.83	0.814	526.0	3 ± 3	$0.8 \pm 0.8 \pm 0.1$	1.1σ	2.6
4.210	5.75	0.821	572.1	-1 ± 1	$-0.2 \pm 0.4 \pm 0.0$	⋯	0.9
4.220	6.99	0.829	569.1	-2 ± 2	$-0.4 \pm 0.4 \pm 0.1$	⋯	0.7
4.230	9.13	0.832	1100.9	0 ± 4	$0.0 \pm 0.3 \pm 0.0$	0.1σ	0.6
4.237	9.71	0.839	530.0	0 ± 3	$0.1 \pm 0.4 \pm 0.0$	0.3σ	1.0
4.246	10.41	0.844	538.1	-3 ± 2	$-0.4 \pm 0.3 \pm 0.1$	⋯	0.5
4.260	11.80	0.848	825.7	-8 ± 4	$-0.6 \pm 0.3 \pm 0.1$	⋯	0.3
4.270	12.19	0.853	531.1	6 ± 4	$0.6 \pm 0.4 \pm 0.1$	1.5σ	1.5
4.290	12.17	0.862	502.4	0 ± 4	$-0.0 \pm 0.4 \pm 0.0$	0.1σ	0.9
4.315	14.79	0.869	501.2	2 ± 6	$0.2 \pm 0.5 \pm 0.0$	0.4σ	0.9
4.340	15.63	0.877	505.0	-8 ± 7	$-0.7 \pm 0.6 \pm 0.1$	⋯	0.6
4.360	17.11	0.884	544.0	-7 ± 9	$-0.5 \pm 0.6 \pm 0.1$	⋯	1.0
4.380	16.19	0.886	522.7	-19 ± 8	$-1.3 \pm 0.6 \pm 0.2$	⋯	1.1
4.400	16.44	0.890	507.8	11 ± 12	$0.8 \pm 0.9 \pm 0.1$	1.0σ	4.6
4.420	18.32	0.895	1090.7	-39 ± 18	$-1.2 \pm 0.6 \pm 0.2$	⋯	0.6
4.440	16.74	0.899	569.9	7 ± 15	$0.5 \pm 0.9 \pm 0.1$	0.5σ	3.1
4.600	19.59	0.922	586.9	31 ± 13	$1.6 \pm 0.7 \pm 0.2$	2.5σ	3.3
4.620	18.48	0.926	521.5	27 ± 13	$1.6 \pm 0.8 \pm 0.2$	2.2σ	3.4
4.640	18.80	0.926	552.4	17 ± 13	$1.0 \pm 0.7 \pm 0.1$	1.4σ	2.3
4.660	19.11	0.929	529.6	13 ± 13	$0.8 \pm 0.7 \pm 0.1$	1.1σ	2.0
4.680	19.09	0.929	1669.3	58 ± 24	$1.0 \pm 0.4 \pm 0.1$	1.8σ	1.5
4.700	19.07	0.931	536.5	1 ± 13	$0.1 \pm 0.7 \pm 0.0$	0.1σ	1.4
4.750	20.05	0.935	367.2	0 ± 10	$-0.1 \pm 0.8 \pm 0.0$	0.1σ	1.4
4.780	20.04	0.936	512.8	15 ± 12	$0.9 \pm 0.7 \pm 0.1$	1.4σ	2.0
4.840	20.52	0.940	527.3	-11 ± 10	$-0.6 \pm 0.5 \pm 0.1$	⋯	0.7
4.916	20.41	0.948	208.1	-6 ± 5	$-0.9 \pm 0.8 \pm 0.1$	⋯	1.1
4.946	20.02	0.950	160.4	-10 ± 3	$-1.7 \pm 0.6 \pm 0.2$	⋯	0.8

where the subscript "MC" represents MC simulation and the subscript "data" represents the data sample, $N^{v}_{\mathrm{signal}_{\mathrm{data(MC)}}}$ is the number of events in the signal region of a selection criterion v, and $N^{v}_{\mathrm{all}_{\mathrm{data(MC)}}}$ is the number of events in the full range of v.

The uncertainty of $\epsilon^{v}_{\mathrm{data(MC)}}$

$$\sigma_{\epsilon^{v}_{\mathrm{data(MC)}}} = \sqrt{\frac{\epsilon^{v}_{\mathrm{data(MC)}}(1-\epsilon^{v}_{\mathrm{data(MC)}})}{N^{v}_{\mathrm{all}_{\mathrm{data(MC)}}}}}, \tag{12}$$

and the uncertainty of f^{v} is

$$\frac{\sigma^{2}_{f^{v}}}{f^{v2}} = \frac{\sigma^{2}_{\epsilon^{v}_{\mathrm{data}}}}{\epsilon^{v\,2}_{\mathrm{data}}} + \frac{\sigma^{2}_{\epsilon^{v}_{\mathrm{MC}}}}{\epsilon^{v\,2}_{\mathrm{MC}}}, \tag{13}$$

since data and MC simulation are independent. For $f^{v} = (1 \pm \Delta f^{v}) \pm \sigma_{f^{v}}$, if $|\frac{\Delta f^{v}}{\sigma_{f^{v}}}| < 1.00$, no correction will be applied and $|\Delta f^{v}| + \sigma_{f^{v}}$ will be taken as the systematic uncertainty, where Δf^{v} is the deviation of f^{v} from 1; while if $|\frac{\Delta f^{v}}{\sigma_{f^{v}}}| > 1.00$, the MC efficiency will be corrected as $\epsilon = \epsilon_{MC} \times f^{v}$, and $\sigma_{f^{v}}$ will be taken as the systematic uncertainty.

In order to avoid effects from statistical uncertainty, only data samples at $\sqrt{s} = 4.340$, 4.360, 4.400, 4.420, 4.440, 4.600, and 4.680 GeV are used to estimate the systematic uncertainty originating from the $M(K^{-}\pi^{+}\pi^{+})$ ($RM(D^{+}\pi^{+}_{d}\pi^{-}_{d})$) mass window requirement. A constant parameter is used to fit the distributions of $f^{M(K^{-}\pi^{+}\pi^{+})}$ ($f^{RM(D^{+}\pi^{+}_{d}\pi^{-}_{d})}$) among the data samples mentioned above, and the fitted $f^{M(K^{-}\pi^{+}\pi^{+})}$ ($f^{RM(D^{+}\pi^{+}_{d}\pi^{-}_{d})}$) and $\sigma_{f^{M(K^{-}\pi^{+}\pi^{+})}}$ ($\sigma_{f^{RM(D^{+}\pi^{+}_{d}\pi^{-}_{d})}}$) values are 0.986 ± 0.003 (0.984 ± 0.005), the value of $|\frac{\Delta f^{M(K^{-}\pi^{+}\pi^{+})}}{\sigma_{f^{M(K^{-}\pi^{+}\pi^{+})}}}|$ ($|\frac{\Delta f^{RM(D^{+}\pi^{+}_{d}\pi^{-}_{d})}}{\sigma_{f^{RM(D^{+}\pi^{+}_{d}\pi^{-}_{d})}}}|$) is 5.6 (2.8), therefore, the systematic uncertainty is taken as 0.3% (0.5%) and $f^{M(K^{-}\pi^{+}\pi^{+})}$ ($f^{RM(D^{+}\pi^{+}_{d}\pi^{-}_{d})}$) is set to be 0.986 (0.984).

In order to avoid effects from the statistical uncertainty, the same set of data samples as mentioned in the previous paragraph is used to estimate the systematic uncertainties originating from the fit range and background shape of $RM(D^{+}\pi^{+}_{d}\pi^{-}_{d})$. The systematic uncertainty coming from the choice of the fit range is estimated by varying the limits of the fit range from (1.75, 1.96) to (1.77, 1.97) GeV/c^{2}. The background shape is varied from the first-order Chebychev polynomial function to a second-order one at $\sqrt{s} = 4.340$ and 4.360 GeV, and the second-order Chebychev polynomial function to the first-order one at $\sqrt{s} = 4.400$, 4.420, 4.440, 4.600, and 4.680 GeV. The largest difference of the cross section compared with the baseline value among the data samples mentioned above is taken as a systematic uncertainty of 1.6% (1.7%) for the fit range (background shape).

The systematic uncertainty stemming from the $p/\bar{p}$ veto, which is caused by the difference in misidentification probability of K to $p/\bar{p}$ between data and MC simulation, is estimated by the control sample of $J/\psi \to K^{0}_{S}K^{-}\pi^{+} +$ c.c. with the BESIII J/ψ sample [44]. The values of $f^{K\nrightarrow p}$ and $\sigma_{f^{K\nrightarrow p}}$ are 0.996 ± 0.003, and the value of $|\frac{\Delta f^{K\nrightarrow p}}{\sigma_{f^{K\nrightarrow p}}}|$ is 1.4, therefore, the systematic uncertainty is taken as 0.3% and $f^{K\nrightarrow p}$ is set to 0.996. Similarly, using the control sample of $e^{+}e^{-} \to \pi^{+}\pi^{-}J/\psi$ at $\sqrt{s} = 4.260$ GeV [45], $f^{L/\Delta_{L}}$ and $f^{V_{xy,z}}$ are estimated by performing a secondary vertex fit on the π^{+} and π^{-} pair and comparing $V_{xy,z}$ of π^{+}, π^{-}, and lepton pair from J/ψ in data and MC simulation, respectively. The values of $f^{L/\Delta_{L}}$ ($f^{V_{xy,z}}$) and $\sigma_{f^{L/\Delta_{L}}}$ ($\sigma_{f^{V_{xy,z}}}$) are 0.992 ± 0.010 (0.997 ± 0.001), $f^{L/\Delta_{L}}$ ($f^{V_{xy,z}}$) is set as 0.992 (0.997), and the systematic uncertainty associated with the $L_{\pi^{+}_{d}\pi^{-}_{d}}/\Delta_{L_{\pi^{+}_{d}\pi^{-}_{d}}}$ requirement for the K^{0}_{S} veto ($V_{xy,z}$ requirements) is 1.0% (0.1%).

$e^{+}e^{-} \to \pi^{+}\pi^{-}\psi(3770) \to \pi^{+}\pi^{-}D^{+}D^{-}$ and $e^{+}e^{-} \to D_{1}(2420)^{+}D^{-} \to \pi^{+}\pi^{-}D^{+}D^{-}$ processes are simulated when estimating ω_{i}, for the estimation of the systematic uncertainty stemming from the $\psi(3770)$ ($D_{1}(2420)^{+}$) shape, alternative MC samples are produced by varying the width of $\psi(3770)$ ($D_{1}(2420)^{+}$) by one standard deviation of its world average value [1]. The difference of the cross section of $e^{+}e^{-} \to \pi^{+}\pi^{-}D^{+}D^{-}$ process compared with the baseline value is taken as the systematic uncertainty as listed in Table VII.

In Sec. II, $e^{+}e^{-}$ is assumed to annihilate into $D_{1}(2420)^{+}D^{-}$ directly with a uniform angular distribution, and the systematic uncertainty stemming from modeling the angular distribution of the $e^{+}e^{-} \to D_{1}(2420)^{+}D^{-}$ process is estimated by repeating the analysis procedure with the new model. For the $e^{+}e^{-} \to D_{1}(2420)^{+}D^{-}$ process, two extreme cases of the angular distribution following $1 + \cos^{2}\theta_{D_{1}}$ and $1 - \cos^{2}\theta_{D_{1}}$ are assumed, where $\theta_{D_{1}}$ is the helicity angle of the $D_{1}(2420)^{+}$ in the rest frame of the initial $e^{+}e^{-}$ system. The fractions of these two cases are estimated by fitting to the $\cos\theta_{D^{+}}$ distribution, where $\theta_{D^{+}}$ is the polar angle of D^{+} in the rest frame of the initial $e^{+}e^{-}$ system, the detection efficiency of $e^{+}e^{-} \to D_{1}(2420)^{+}D^{-} \to \pi^{+}\pi^{-}D^{+}D^{-}$ process is recalculated according to the detection efficiencies and fractions of these two cases, and the cross section of $e^{+}e^{-} \to \pi^{+}\pi^{-}D^{+}D^{-}$ process is recalculated as well. The difference of the cross section of the $e^{+}e^{-} \to \pi^{+}\pi^{-}D^{+}D^{-}$ process compared with the baseline value is taken as the systematic uncertainty as listed in Table VII.

In Sec. III, the normalization factor f_{1} (f_{2}) in the B sample is estimated by assuming a linear background distribution in $M(K^{-}\pi^{+}\pi^{+})$ ($RM(D^{+}\pi^{+}_{d}\pi^{-}_{d})$). A second-order Chebychev polynomial function is used as the

background shape to fit the $M(K^-\pi^+\pi^+)$ ($RM(D^+\pi_d^+\pi_d^-)$) distribution to estimate f_1 (f_2). The signal shape is modeled by the $M(K^-\pi^+\pi^+)$ ($RM(D^+\pi_d^+\pi_d^-)$) distributions in MC simulation of each subprocess weighted according to fractions of each subprocess, ω_i, and convolved with a Gaussian function to take the resolution difference between data and MC simulation into consideration. ω_i is reestimated according to the new f_1 and f_2, and the cross section of the $e^+e^- \to \pi^+\pi^- D^+ D^-$ process is recalculated. The difference from the baseline value is taken as the systematic uncertainty originating from this source as listed in Table VII.

The systematic uncertainty due to the uncertainty of the fraction of each subprocess, ω_i, is estimated by varying ω_i 500 times according to the covariant matrix in the simultaneous fit of $RM(D^+)$, $RM(D^-_{\rm miss})$, and $RM(\pi_d^+\pi_d^-)$ distributions for each $\sqrt{s}$. In each iteration, the difference between the cross section of the $e^+e^- \to \pi^+\pi^- D^+ D^-$ process and the baseline value is calculated, and the distribution of the differences is sampled at each $\sqrt{s}$, the standard deviation of the distribution is taken as the systematic uncertainty as listed in Table VII.

The systematic uncertainty of the radiative correction is calculated by using the KKMC package. Initially, the observed signal events are assumed to originate from the

TABLE VII. Systematic uncertainties (%) from the scale factors f_1 and f_2 (f_1 and f_2), $\psi(3770)$, and $D_1(2420)^+$ shapes, including a new Breit-Wigner shape in the high energy region when parametrizing each subprocess cross section line shape, uncertainty of ω_i (ω_i), and angular distribution modeling of $e^+e^- \to D_1(2420)^+ D^-$ decay (HELAMP). The last column shows the total systematic uncertainty obtained by summing up all sources of systematic uncertainties in quadrature assuming they are uncorrelated.

$\sqrt{s}^{\rm nominal}$	f_1 and f_2	$\psi(3770)$ shape	$D_1(2420)^+$ shape	New Breit-Wigner	ω_i	HELAMP	Total
4.190	0.0	0.0	···	0.0	14.4	···	16.6
4.200	0.0	0.0	···	0.0	19.3	···	21.0
4.210	0.0	0.0	···	0.0	16.8	···	18.7
4.220	0.0	0.0	···	0.0	0.8	···	8.3
4.230	0.6	1.7	···	0.9	0.8	···	8.6
4.237	0.0	1.6	···	2.3	0.6	···	8.8
4.245	0.5	0.3	···	0.3	1.8	···	8.5
4.246	0.5	0.7	···	3.0	7.8	···	11.8
4.260	0.2	0.9	···	0.7	0.4	···	8.4
4.270	0.0	0.5	···	1.2	0.7	···	8.4
4.280	0.2	1.4	···	1.4	0.5	···	8.5
4.290	0.1	0.1	···	1.8	0.5	···	8.5
4.310	1.5	0.3	···	1.4	0.4	···	8.5
4.315	0.1	0.4	···	0.3	0.2	···	8.3
4.340	0.1	0.4	0.7	1.2	0.3	0.5	8.4
4.360	0.2	0.0	0.2	2.0	0.1	0.2	8.5
4.380	0.2	0.6	0.1	0.4	0.3	0.8	8.4
4.390	0.1	0.3	1.2	1.0	0.8	0.3	8.5
4.400	0.1	0.5	1.0	0.1	0.7	0.6	8.4
4.420	0.0	0.1	0.6	0.1	1.8	0.8	8.5
4.440	0.2	0.9	3.3	0.2	1.5	0.4	9.1
4.470	0.2	1.4	0.9	0.5	6.6	0.2	10.7
4.530	0.2	0.2	0.4	0.3	6.0	0.7	10.3
4.575	0.5	0.3	1.8	0.0	2.1	1.3	8.8
4.600	0.5	0.4	1.7	2.8	0.8	0.8	9.0
4.612	0.1	0.2	0.0	0.3	1.2	0.5	8.4
4.620	0.1	1.5	0.9	0.3	1.1	0.4	8.5
4.640	0.5	0.2	0.8	1.6	1.4	0.2	8.6
4.660	0.2	0.9	0.3	2.6	1.0	0.2	8.8
4.680	0.2	0.4	0.9	0.0	0.4	0.1	8.3
4.700	0.0	0.8	0.7	2.3	0.5	0.0	8.7
4.740	0.1	0.1	2.1	0.5	0.8	0.3	8.6
4.750	0.5	0.8	0.6	1.9	1.2	0.2	8.7
4.780	0.1	0.3	0.2	0.4	0.8	0.3	8.3
4.840	0.3	0.9	0.7	0.5	0.6	1.9	8.6
4.914	0.0	0.6	1.1	1.1	1.4	1.7	8.7
4.946	0.8	0.6	0.4	0.6	1.6	0.9	8.6

$Y(4260)$ resonance to obtain the efficiency and ISR correction factor. Then, the measured line shape is used as input to calculate the efficiency and ISR correction factor again. This procedure is repeated until the difference between the subsequent iteration is comparable with the statistical uncertainty. The systematic uncertainty due to the input line shapes of subprocesses is estimated as described below.

The input line shape of each subprocess is varied 500 times according to the convariant matrix when parametrizing, and the $\sum \omega_i \epsilon_i (1+\delta)_i$ distribution is sampled at $\sqrt{s} = 4.380$, 4.390, 4.400, 4.420, and 4.440 GeV. The maximum fraction of width and mean values of the distributions, 2.8%, is taken as the systematic uncertainty due to the input line shapes in the ISR correction. Moreover, new resonances around $\sqrt{s} = 4.7$ GeV are added when parametrizing the line shape of each subprocess since there is an evidence around $\sqrt{s} = 4.7$ GeV in the $e^+e^- \to \pi^+\pi^- D^+ D^-$ cross section line shape, and the difference is taken as the systematic uncertainty associated with the new BW resonance in the high energy regions as listed in Table VII.

Table VII summarizes the total systematic uncertainties. The total systematic uncertainty at each $\sqrt{s}$ is obtained by summing up all sources of systematic uncertainties in quadrature, assuming that they are uncorrelated.

B. Systematic uncertainties in R_0 parameters

The systematic uncertainties when parametrizing R_0 in the $e^+e^- \to \pi^+\pi^- D^+ D^-$ cross section line shape mainly stem from the absolute $\sqrt{s}$ measurement, the $\sqrt{s}$ spread, global shift of the $\sqrt{s}$ for data samples taken in the same period, additional R_1, or Φ_4, or both of them, and the systematic uncertainty of the cross section measurement.

The absolute $\sqrt{s}$ of data samples with $\sqrt{s}$ smaller than 4.610 GeV are measured with dimuon events, with an uncertainty of ± 0.8 MeV, while those with $\sqrt{s}$ larger than or equal to 4.610 GeV are measured with $\Lambda_c^+ \bar{\Lambda}_c^-$ events with an uncertainty of ± 0.6 MeV. Thus, 0.8 MeV is taken as the systematic uncertainty, and propagates to the mass of R_0 by the same amount.

The systematic uncertainty from the $\sqrt{s}$ spread is estimated by convolving the fit formula with a Gaussian function with a width of 1.6 MeV, which is the energy spread, determined from measurement results of the beam energy measurement system [46] at other $\sqrt{s}$.

The systematic uncertainty from global shift of the $\sqrt{s}$ for data samples taken in the same period is estimated by shifting the $\sqrt{s}$ of corresponding data samples by 3 MeV and deviations of parameters is taken as the systematic uncertainties.

The systematic uncertainties from the additional R_1, or Φ_4, or both of them are estimated by comparing the differences of R_0 paramteters obtained from Figs. 8(a) and 8(b), Figs. 8(a) and 8(c), and Figs. 8(a) and 8(d), respectively. We take the maximum difference between the central values and add the statistical uncertainty of the alternative fit linearly as a conservative estimation of the systematic uncertainty when there are multiple solutions.

TABLE VIII. Systematic uncertainties in the measurement of R_0 parameters. $\sqrt{s}$ measurement represents the systematic uncertainty from the center-of-mass measurement. $\sqrt{s}$ shift represents the systematic uncertainty from the global shift of $\sqrt{s}$ for data samples taken in the same period. Cross section$_{\mathrm{a(b)}}$ represents the systematic uncertainty from the cross section measurements which are uncorrelated (common) in each data sample. R_1 represents the systematic uncertainty from additional BW function. Φ_4 represents the systematic uncertainty from additional phase space term. $R_1 + \Phi_4$ represents the systematic uncertainty from additional BW function and phase space term.

Sources	m_0 (MeV/c^2)	Γ_0^{tot} (MeV)	$\Gamma_0^{e^+e^-}\mathcal{B}_0$ (eV)
$\sqrt{s}$ measurement	0.8	...	...
$\sqrt{s}$ shift	1.9	1	0.1
$\sqrt{s}$ spread	0.0	0	1.4
Cross section$_{\mathrm{a}}$	0.1	2	0.1
Cross section$_{\mathrm{b}}$	...	...	1.0
R_1	6.4	14	+21.0
Φ_4	0.5	19	−3.7
$R_1 + \Phi_4$	6.3	16	+13.1
Overall	9.2	29	$^{+21.1}_{-4.4}$

The systematic uncertainty from the cross section measurement is divided into two parts. The first part covers uncorrelated systematic uncertainties among the different data samples (those in Table VII). The corresponding systematic uncertainty is estimated by including the uncertainty in the fit to the cross section, and taking the differences on the parameters as the systematic uncertainties. The second part includes all the other systematic uncertainties (8.3%), which is common for all data samples, only affects the $\Gamma_0^{e^+e^-}\mathcal{B}_0$ measurement, and does not affect mass and width of R_0.

Table VIII summarizes the systematic uncertainties in the parameters of resonances. The total systematic uncertainty is obtained by summing up all sources of systematic uncertainties in quadrature, assuming they are uncorrelated.

C. Systematic uncertainties in $X(3842)$ measurement

Except for the fit range and the background shape of the $RM(\pi_d^+\pi_d^-)$, $RM(D^+)$, and $RM(D^-_{\mathrm{miss}})$ mass window requirements, other sources of systematic uncertainties associated with this measurement are the same as those in Sec. VII A, but with the fit range and background shape of $RM(D^+\pi_d^+\pi_d^-)$ excluded.

The systematic uncertainty originating from the fit range of $RM(\pi_d^+\pi_d^-)$ is estimated by varying the limits of the fit range from $(3.79, 3.89)$ to $(3.81, 3.91)$ GeV/c^2. The

difference of the cross section from the baseline value in the data sample at $\sqrt{s} = 4.680$ GeV is taken as the systematic uncertainty, and is 10.4%. The background shape is varied from a second-order Chebychev polynomial function to a first order one in the data sample taken at $\sqrt{s} = 4.680$ GeV, the difference of the cross section compared with the baseline value is taken as the systematic uncertainty, and is 1.9%.

The systematic uncertainty stemming from the $RM(D^+)$ and $RM(D^-_{\rm miss})$ mass window requirements, which is mainly caused by the difference between distributions of data and MC simulation in the corresponding selection criterion ranges, is estimated by producing alternative MC samples where the mass and width of $f_0(500)$ are varied by one standard deviation in the data sample at $\sqrt{s} = 4.680$ GeV. The difference of the cross section compared with the baseline value is taken as the systematic uncertainty, and is 1.9%.

The total systematic uncertainties for data samples with $\sqrt{s}$ smaller than or equal to 4.315 GeV are equal to 12.9%, and for those with $\sqrt{s}$ larger than 4.315 GeV are equal to 13.1% by summing up all sources of systematic uncertainties in quadrature, assuming they are uncorrelated.

VIII. SUMMARY

Using data samples taken at $\sqrt{s}$ from 4.190 to 4.946 GeV, the cross section of the $e^+e^- \to \pi^+\pi^- D^+ D^-$ process is reported for the first time by a partial reconstruction method.

By fitting the $e^+e^- \to \pi^+\pi^- D^+ D^-$ cross section line shape, we observe a resonance with a mass of $(4371.6 \pm 2.5 \pm 9.2)$ MeV/c^2 and a width of $(167 \pm 4 \pm 29)$ MeV, which is in agreement with the $\psi(4360)$ or $Y(4390)$ state, and we determine the product of its electronic partial width and its decay branching fraction to $\pi^+\pi^- D^+ D^-$ as $(12 \pm 0^{+21}_{-4})$ eV, where the first uncertainties are statistical and the second are systematic. There is evidence with a statistical significance of 4.7σ for a second resonance, or a statistical significance of 3.8σ for a nonresonance amplitude, or both of them.

The $X(3842)$ resonance is searched for in the $RM(\pi^+_d\pi^-_d)$ distribution and evidence is found in the $M(\pi^+_d\pi^-_d)$ distribution in data samples with $\sqrt{s}$ from 4.600 to 4.700 GeV, and its significance is 4.2σ. By comparing this study with previous studies, the cross section of the $e^+e^- \to \pi^+\pi^-\psi(3770) \to \pi^+\pi^- D^+ D^-$ process peaks around 4.390 GeV, which indicates this process might be produced via the $Y(4390)$ state [22,23]; the process $e^+e^- \to \pi^+\pi^-\psi_2(3823)(\to \gamma\chi_{c1})$ peaks around $\sqrt{s} = 4.360$ and 4.420 GeV, which means this process might be produced via the $Y(4360)$ and the $\psi(4415)$ [24] resonances. There is evidence that the cross section of the $e^+e^- \to \pi^+\pi^- X(3842)$ process peaks at $\sqrt{s}$ from 4.600 to 4.700 GeV, but no significant signal is observed in samples collected at $\sqrt{s}$ around 4.400 GeV. This indicates that the production mechanism of the $e^+e^- \to \pi^+\pi^-\psi(1D)$ processes might be different and could proceed via different Y or ψ states. More data samples and more precise measurements are needed to reveal the mechanism [47].

ACKNOWLEDGMENTS

The BESIII collaboration thanks the staff of BEPCII and the IHEP computing center for their strong support. This work is supported in part by National Key R&D Program of China under Contracts No. 2020YFA0406300 and No. 2020YFA0406400; National Natural Science Foundation of China (NSFC) under Contracts No. 11635010, 11735014, 11835012, 11935015, 11935016, 11935018, 11961141012, 12022510, 12025502, 12035009, 12035013, 12192260, 12192261, 12192262, 12192263, 12192264, 12192265; the Chinese Academy of Sciences (CAS) Large-Scale Scientific Facility Program; Joint Large-Scale Scientific Facility Funds of the NSFC and CAS under Contract No. U1832207; CAS Key Research Program of Frontier Sciences under Contract No. QYZDJ-SSW-SLH040; 100 Talents Program of CAS; INPAC and Shanghai Key Laboratory for Particle Physics and Cosmology; ERC under Contract No. 758462; European Union's Horizon 2020 research and innovation programme under Marie Sklodowska-Curie grant agreement under Contract No. 894790; German Research Foundation DFG under Contract No. 443159800, Collaborative Research Center CRC 1044, GRK 2149; Istituto Nazionale di Fisica Nucleare, Italy; Ministry of Development of Turkey under Contract No. DPT2006K-120470; National Science and Technology fund; National Science Research and Innovation Fund (NSRF) via the Program Management Unit for Human Resources and Institutional Development, Research and Innovation under Contract No. B16F640076; STFC (United Kingdom); Suranaree University of Technology (SUT), Thailand Science Research and Innovation (TSRI), and National Science Research and Innovation Fund (NSRF) under Contract No. 160355; The Royal Society, UK under Contracts No. DH140054 and No. DH160214; The Swedish Research Council; U.S. Department of Energy under Contract No. DE-FG02-05ER41374.

[1] P. A. Zyla *et al.* (Particle Data Group), Prog. Theor. Exp. Phys. **2020**, 083C01 (2020) and 2021 update.
[2] N. Brambilla, A. Pineda, J. Soto, and A. Vairo, Rev. Mod. Phys. **77**, 1423 (2005).
[3] N. Brambilla *et al.*, Eur. Phys. J. C **71**, 1534 (2011).
[4] N. Brambilla, S. Eidelman, P. Foka, S. Gardner, A. S. Kronfeld, M. G. Alford, R. Alkofer, M. Butenschoen, T. D. Cohen, J. Erdmenger *et al.*, Eur. Phys. J. C **74**, 2981 (2014).
[5] E. Eichten, K. Gottfried, T. Kinoshita, K. D. Lane, and T. M. Yan, Phys. Rev. D **17**, 3090 (1978).
[6] S. Godfrey and N. Isgur, Phys. Rev. D **32**, 189 (1985).
[7] T. Barnes, S. Godfrey, and E. S. Swanson, Phys. Rev. D **72**, 054026 (2005).
[8] M. Ablikim *et al.* (BES Collaboration), Phys. Lett. B **660**, 315 (2008).
[9] A. J. Bevan *et al.* (*BABAR* and Belle Collaborations), Eur. Phys. J. C **74**, 3026 (2014).
[10] B. Aubert *et al.* (*BABAR* Collaboration), Phys. Rev. Lett. **95**, 142001 (2005).
[11] B. Aubert *et al.* (*BABAR* Collaboration), Phys. Rev. Lett. **98**, 212001 (2007).
[12] X. L. Wang *et al.* (Belle Collaboration), Phys. Rev. Lett. **99**, 142002 (2007).
[13] T. V. Uglov, Y. S. Kalashnikova, A. V. Nefediev, G. V. Pakhlova, and P. N. Pakhlov, JETP Lett. **105**, 1 (2017).
[14] N. Brambilla, S. Eidelman, C. Hanhart, A. Nefediev, C. P. Shen, C. E. Thomas, A. Vairo, and C. Z. Yuan, Phys. Rep. **873**, 1 (2020).
[15] F. K. Guo, C. Hanhart, Ulf-G. Meißner, Q. Wang, Q. Zhao, and B. S. Zou, Rev. Mod. Phys. **90**, 015004 (2018).
[16] H. X. Chen, W. Chen, X. Liu, and S. L. Zhu, Phys. Rep. **639**, 1 (2016).
[17] A. J. Bevan *et al.* (*BABAR* and Belle Collaborations), Eur. Phys. J. C. **74**, 3026 (2014).
[18] M. Ablikim *et al.* (BESIII Collaboration), Chin. Phys. C **42**, 083001 (2018).
[19] M. Ablikim *et al.* (BESIII Collaboration), Phys. Rev. D **101**, 112008 (2020).
[20] M. Ablikim *et al.* (BESIII Collaboration), Phys. Rev. D **104**, 032012 (2021).
[21] M. Ablikim *et al.* (BESIII Collaboration), Phys. Rev. Lett. **122**, 102002 (2019).
[22] M. Ablikim *et al.* (BESIII Collaboration), Phys. Lett. B **804**, 135395 (2020).
[23] M. Ablikim *et al.* (BESIII Collaboration), Phys. Rev. D **100**, 032005 (2019).
[24] M. Ablikim *et al.* (BESIII Collaboration), Phys. Rev. Lett. **115**, 011803 (2015).
[25] R. Aaij *et al.* (LHCb Collaboration), J. High Energy Phys. 07 (2019) 035.
[26] M. Ablikim *et al.* (BESIII Collaboration), Nucl. Instrum. Methods Phys. Res., Sect. A **614**, 345 (2010).
[27] C. H. Yu *et al.*, in *Proceedings of the IPAC2016, Busan, Korea, 2016* (JACoW Publishing, Geneva, Switzerland, 2016).
[28] X. Li *et al.*, Radiat. Detect. Technol. Methods **1**, 13 (2017); Y. X. Guo *et al.*, Radiat. Detect. Technol. Methods **1**, 15 (2017); P. Cao *et al.*, Nucl. Instrum. Methods Phys. Res., Sect. A **953**, 163053 (2020).
[29] M. Ablikim *et al.* (BESIII Collaboration), Chin. Phys. C **40**, 063001 (2016).
[30] M. Ablikim *et al.* (BESIII Collaboration), Chin. Phys. C **45**, 103001 (2021).
[31] M. Ablikim *et al.* (BESIII Collaboration), arXiv:2203.04289.
[32] M. Ablikim *et al.* (BESIII Collaboration), arXiv:2203.03133.
[33] M. Ablikim *et al.* (BESIII Collaboration), Chin. Phys. C **39**, 093001 (2015).
[34] S. Agostinelli *et al.* (GEANT4 Collaboration), Nucl. Instrum. Methods Phys. Res., Sect. A **506**, 250 (2003).
[35] S. Jadach, B. F. L. Ward, and Z. Was, Comput. Phys. Commun. **130**, 260 (2000); Phys. Rev. D **63**, 113009 (2001).
[36] D. J. Lange, Nucl. Instrum. Methods Phys. Res., Sect. A **462**, 152 (2001); R. G. Ping, Chin. Phys. C **32**, 599 (2008).
[37] J. C. Chen, G. S. Huang, X. R. Qi, D. H. Zhang, and Y. S. Zhu, Phys. Rev. D **62**, 034003 (2000); R. L. Yang, R. G. Ping, and H. Chen, Chin. Phys. Lett. **31**, 061301 (2014).
[38] P. Golonka and Z. Was, Eur. Phys. J. C **45**, 97 (2006).
[39] J. Conrad, O. Botner, A. Hallgren, and C. Pérez de los Heros, Phys. Rev. D **67**, 012002 (2003).
[40] E. M. Aitala *et al.* (Fermilab E791 Collaboration), Phys. Rev. Lett. **86**, 770 (2001).
[41] M. Ablikim *et al.* (BESIII Collaboration), Phys. Rev. D **101**, 112008 (2020).
[42] M. Ablikim *et al.* (BESIII Collaboration), Phys. Rev. Lett. **110**, 252001 (2013).
[43] S. Actis *et al.*, Eur. Phys. J. C **66**, 585 (2010).
[44] M. Ablikim *et al.* (BESIII Collaboration), Phys. Rev. Lett. **126**, 092002 (2021).
[45] M. Ablikim *et al.* (BESIII Collaboration), Phys. Rev. Lett. **118**, 092001 (2017).
[46] E. V. Abakumova *et al.*, Nucl. Instrum. Methods Phys. Res., Sect. A **659**, 21 (2011).
[47] M. Ablikim *et al.* (BESIII Collaboration), Chin. Phys. C **44**, 040001 (2020).